Improved Kalman-based attitude estimation framework for UAVs via an antenna array

Thiago Felippe K. Cordeiro [a,b,*], João Paulo C.L. da Costa [a,c,d],
Rafael Timóteo de Sousa Júnior [a], Hing Cheung So [e], Geovany A. Borges [a]

[a] Department of Electrical Engineering, University of Brasília, Brazil
[b] Aerospace Department, University of Brasília, Brazil
[c] Institute for Information Technology, Ilmenau University of Technology, Ilmenau, Germany
[d] Fraunhofer Institute for Integrated Circuits IIS, Erlangen, Germany
[e] Department of Electronic Engineering, City University of Hong Kong, Hong Kong

ARTICLE INFO

ABSTRACT

Accurate attitude estimation is crucial for Unmanned Aerial Vehicles (UAVs) in order to facilitate automated activities such as landing or trajectory tracking. Recently antenna array based communication systems have been installed in UAVs. This array structure can also be applied for attitude estimation by computing the line-of-sight (LOS) path between the base station and UAV. In this paper, we propose a complete framework for attitude estimation by exploiting 3D LOS vector obtained from the antenna array system. We present all the steps to incorporate the estimated LOS vector into the TRIaxial Attitude Determination (TRIAD), QUaternion ESTimator (QUEST) and Kalman algorithms. As an additional contribution, the error covariance matrix of the LOS vector is analytically calculated by first finding the phase shift mean squared error using the known perturbation model from Singular Value Decomposition and assuming that the antenna array measured data error can be modeled as a circularly symmetric white noise. We evaluate five array configurations via Monte Carlo simulations. We show that array configurations that provide orthogonal components of the LOS vector achieve a better performance. The usage of more than three pairs of antennas to improve the estimation of the LOS vector is also proposed for low and intermediate signal-to-noise ratio regimes.

© 2016 Elsevier Inc. All rights reserved.

1. Introduction

Attitude, also known as pose, corresponds to the orientation of an object, e.g., a Unmanned Aerial Vehicle (UAV), with respect to some reference, such as the horizon plane and the north direction. Mathematically, the attitude is described by the relationship between two coordinate frames: a frame fixed in the UAV, known as the body frame S_b, and the North-East-Down (NED) reference frame S_{NED}.

Attitude estimation is important in several UAV's automated tasks, such as waypoint following [1], target tracking [2], rendezvous between UAVs [2], formation flight [3,4] and automated aerial refueling [5].

Vector-defined properties, such as in magnetic or gravitational fields, depend on the frames and are used for attitude estimation. While the S_{NED} representation of a vector-defined property is assumed to be known, the S_b representation can be provided from the signals of specialized sensors. Once measurements are obtained by at least two types of different sensors, several algorithms can be applied for attitude estimation, which include Triaxial Attitude Determination (TRIAD) [6], Quaternion Estimator (QUEST) [6], and Extended Kalman Filter (EKF) [7,8].

Examples of traditional sensors for attitude estimation are magnetometers, accelerometers and cameras. Magnetometers measure the magnetic field direction with respect to the Earth magnetic north pole [9–11], whereas accelerometers measure the gravity vector direction [9]. Cameras can be used to point and track points of interest.

The magnetometer is a low-cost sensor [10], and provides a very high sampling rate measurement [11]. However, the measurements are significantly affected by near metal structures, e.g., the vehicle structure, and a calibration process [11] is required to compensate such influence. In addition, the magnetometer is affected

* Corresponding author.
E-mail addresses: thiagocordeiro@unb.br (T.F.K. Cordeiro),
joaopaulo.dacosta@ene.unb.br (J.P.C.L. da Costa), desousa@unb.br (R.T. de Sousa),
hcso@ee.cityu.edu.hk (H.C. So), gaborges@unb.br (G.A. Borges).

by electromagnetic or other time-varying interferences, generated by, e.g., electrical components of the vehicle, which can be difficult to compensate [11]. Finally, the true magnetic field must be known. Earth's magnetic field can be accurately estimated by using the International Geomagnetic Reference Field (IGRF) model [12]. However, near Earth's surface, such as in very low altitude flights, artificial and natural sources of metal or electromagnetic interference, such as buildings, magnetized crust rocks, voltage transformers and lightning, can locally distort the magnetic field, which is not accounted by the IGRF model [13].

Accelerometers are usually present in UAVs as a component of the inertial measurement unit (IMU). Microelectromechanical system (MEMS) type accelerometer has similar cost and sampling rate to magnetometers. However, accelerometers are affected by non-gravitational accelerations generated by maneuvers or Coriolis effect [9,14]. These non-gravitational accelerations can be detected and the corresponding corrupted measurement can be rejected [14], or can be partially compensated by the use of extra sensors, such as GPS and gyro. However, the side effect is the increment of the measurement noise covariance [9].

There are several camera-based attitude estimation approaches. Some examples are to use a camera to track known landmarks to obtain the line-of-sight (LOS) vector between the UAV and these locations [15] or to find the horizon line. This approach is similar to what human pilots do. However, in comparison with magnetometers and accelerometers, the camera-based approach is more computationally intense. Moreover, the camera cannot track if the object is occluded or too far away or if it is night or a foggy day. A new research topic related to camera is the estimation of the relative attitude between a leader and a follower UAV [2,4,5]. Relative attitude estimation goes beyond the scope of this paper. Therefore, we do not consider relative attitude estimation schemes in this work.

With antenna arrays being installed in UAVs to improve communication to base stations, we propose to exploit such antenna arrays for attitude estimation without additional hardware cost. The proposed approach can be combined with current sensors, such as magnetometer and accelerometer, or replace one of them depending on the scenario.

The patented Wireless Local Positioning System (WLPS) [16] is a localization system, which uses only one antenna array known as dynamic base station (DBS) and estimates time-of-arrival (TOA) and direction-of-arrival (DOA) in order to locate any cooperative antenna, called transceiver (TRX). Its TOA is obtained by measuring the time between transmitting a pre-determined digital signal, and its reception in a two-way link. The DOA in WLPS is obtained by the use of an antenna array at the DBS.

In [17,18], the set of reference antennas, i.e. DBS in WLPS, has known static position, while a mobile single antenna element has unknown position. The orientation of the DBS antennas is known. In [19–21] the DBS antenna array is located at the moving object, with unknown position. The attitude, however, is assumed as perfectly known. Note that in this work the goal is the attitude estimation and, for this task, we propose a framework that exploits the DOA information.

In our previous works, a cross-shaped four element antenna array [22,23], a cross-shaped six element antenna array [23,24] and a hexagon-shaped seven element electronically steerable parasitic antenna radiator (ESPAR) array [25] are proposed for UAV attitude estimation. Except by [24], these works exploit a set of non-linear attitude dependent equations that describe the relative position between the UAV antennas and the ground antenna. These non-linear equations are numerically and analytically solved in [22,23] and in [25], respectively.

In [24], we propose to use the DOA estimates from an antenna array system as a unitary-norm vector in S_b instead of a pair of

angles, i.e., the Cartesian coordinate system replaces the polar one. Such approach allows to incorporate known attitude estimation algorithms, such as TRIAD and EKF, into our antenna array based framework. As discussed in [24], this technique is more robust against noise and has less singularity points when compared with our previous schemes [22,23,25].

In order to apply the EKF, the error covariance of the phase shift estimate is required. In [24], the error covariance is assumed constant. In practice, for array based attitude estimation systems, the error covariance can be obtained in a previous calibration process by comparing the true phase shifts with the ESPRIT-estimated ones via Monte Carlo trials. However, such calibration is not robust due to the restriction to a specific scenario and due to the variations of the calculated covariance.

In this paper, we propose an antenna array based attitude estimation framework by extending [24]. First we relax the assumption of a specific scenario by incorporating the algorithm from [26] to estimate the error covariance. Such incorporation removes the need of a calibration process before using the estimator. Another improvement over [24] is the use of less antennas, namely, reducing from six to four, while obtaining similar performance. Such achievement is only possible by locating the antennas in specific parts of the UAV. Therefore, we also relax the restriction on how to physically position and align the antennas in the UAV incurring a possible penalty in terms of performance. Another contribution is to consider combinations of pairs of antennas resulting into more than three phase shifts. In a noiseless scenario, the LOS vector can be completely defined with the use of three pairs of antennas. However, as we show in this work, in low signal-to-noise ratio (SNR) regimes, redundant estimates of phase shifts can increase the precision of the estimated LOS vector.

This paper is divided into eight sections including this introduction. In Section 2, we overview basic concepts and definitions on the coordinate systems and attitude. In Section 3, we show how to obtain the measurement vectors from a magnetometer and from an antenna array system. In Section 4, we propose TRIAD, QUEST and Kalman-based attitude framework incorporating the proposed antenna array LOS as well as the magnetometer. In Section 5, we propose the error covariance estimator for attitude estimation based on the ESPRIT algorithm. In Section 6, we propose different antenna array designs to improve the estimation of the LOS vector. In Section 7, the results of our Monte Carlo simulation campaign are presented considering a UAV moving around a base station. Section 8 concludes this paper.

2. Coordinate systems and attitude

The attitude of a UAV can be formally described as an angular relationship between two frames, namely, the S_b body frame and the S_{NED} North-East-Down frame. The S_b is fixed at the UAV, therefore, it moves and rotates in space with the vehicle, and can be used to represent positions of parts of the UAV (e.g., antennas) and measurements made by sensors fixed in the vehicle (e.g., magnetometer, IMU). On the other hand, the S_{NED} frame is based on the directions of north and vertical (or horizon line) at the UAV position. The S_{NED} axes, namely, $\boldsymbol{n}$, $\boldsymbol{e}$, and $\boldsymbol{d}$ are orthonormal vectors directed, respectively, to the north, east and to the center of Earth, whereas S_b axes, $\boldsymbol{x}_b$, $\boldsymbol{y}_b$, and $\boldsymbol{z}_b$ are orthonormal vectors originated on the center of mass of the UAV and directed, respectively, forward to the right and to the bottom of the vehicle.

Let $\boldsymbol{v}$ be a vector represented in a chosen frame given by a subscript. For instance, $\boldsymbol{v}_{\text{NED}}$ and $\boldsymbol{v}_b$ are representations of the same vector considering the frames S_{NED} and S_b, respectively.

We can obtain $\boldsymbol{v}_b$ by applying a rotation in $\boldsymbol{v}_{\text{NED}}$. These vector rotations can be calculated by the linear transformation matrix $\boldsymbol{D}_b^{\text{NED}} \in \mathbb{R}^{3 \times 3}$, which is called rotational matrix or DCM, and is an orthonormal matrix that changes the reference from S_{NED} to S_b:

$$\boldsymbol{v}_b = \boldsymbol{D}_b^{NED} \cdot \boldsymbol{v}_{NED}. \qquad (1)$$

The inverse transformation can be performed by $\boldsymbol{D}_{NED}^b = (\boldsymbol{D}_b^{NED})^T$:

$$\boldsymbol{v}_{NED} = \boldsymbol{D}_{NED}^b \cdot \boldsymbol{v}_b. \qquad (2)$$

As shown in [27], we can generalize a transformation $\boldsymbol{D}_y^x$ from any frame S_x to another S_y by defining it as

$$\boldsymbol{D}_y^x = \left[[\boldsymbol{x}_1]_y \; [\boldsymbol{x}_2]_y \; [\boldsymbol{x}_3]_y \right], \qquad (3)$$

where $[\boldsymbol{x}_i]_y$ is the i-th S_x basis vector represented on S_y basis. This generalization is used in this work to represent a non-orthogonal frame for different antenna array configurations. The inverse transformation matrix, $\boldsymbol{D}_x^y$, is equal to $(\boldsymbol{D}_y^x)^{-1}$. The relationship $\boldsymbol{D}_x^y = (\boldsymbol{D}_y^x)^T$ holds only when both bases are orthonormal.

Another way to describe attitude is by a rotational quaternion, which is a four-element vector with unitary norm. These four elements can be split into two parts. The first part is called scalar (or real) part q_1 and the remaining component is called vector (or imaginary) part $\boldsymbol{\rho} = [q_2 \; q_3 \; q_4]^T$. Analogous to [3,7–10,15], this work uses the quaternion attitude representation in the EKF attitude estimator. A discussion of the benefits and drawbacks of this representation related to the others can be found in navigation, guidance and control books, such as [28].

Each attitude representation can be converted to any other as shown in [8,28].

3. Data model of measurement vectors

In this section, we show the data model of the measurement vectors using the definitions in Section 2. In Subsection 3.1, we consider the measurement vector obtained by a magnetometer, while, in Subsection 3.2, the measurement vector obtained by an antenna array is considered.

3.1. Magnetometer and magnetic field vector

In this work, the magnetometer is combined with the antenna array as one of the two necessary sensors for the vector measurements. Being the antenna array the main focus of this work, we adopt a simplified model for the magnetometer, which assumes that the magnetic field points to the geographical north and that the magnetic field has unitary norm. Therefore, the magnetic field, which is aligned with the $\boldsymbol{n}$ reference vector of the S_{NED} frame, is given by

$$\boldsymbol{m}_{NED} = [1 \quad 0 \quad 0]^T. \qquad (4)$$

A more complex model for the magnetic field can be found in [29].

By considering (1), we can mathematically model the measurement vector $\boldsymbol{m}_b$ from the magnetometer by using the $\boldsymbol{m}_{NED}$ plus additive noise $\boldsymbol{v}_m$ as follows

$$\boldsymbol{m}_b = \boldsymbol{D}_b^{NED} \cdot \boldsymbol{m}_{NED} + \boldsymbol{v}_m, \qquad (5)$$

where $\boldsymbol{v}_m \in \mathbb{R}^{3 \times 1}$ is an i.i.d. zero mean Gaussian random vector that represents the measurement errors in the magnetic components $\boldsymbol{x}_b$, $\boldsymbol{y}_b$ and $\boldsymbol{z}_b$. The covariance matrix of $\boldsymbol{v}_m$ is given by $\boldsymbol{R}_m$ and is a diagonal matrix with variance σ_m^2 in the main diagonal. Practical values for σ_m^2 can be found on the sensor datasheet.

3.2. Antenna array and LOS vector

In [24], the DOA estimates provided by the antenna array are used to measure the LOS vector $\boldsymbol{d}$ connecting the base station to the UAV. As depicted in Fig. 1, the antenna array measures $\boldsymbol{d}_b$, which is the LOS vector represented in the S_b frame.
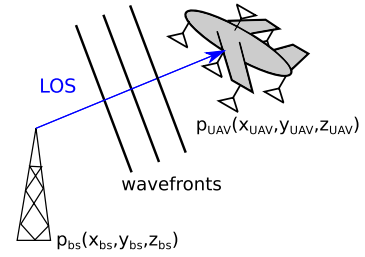

Fig. 1. A base station transmitting data to an antenna array on a UAV. The LOS vector is given by the difference between the position vector of the UAV $\boldsymbol{p}_{UAV}$ and the position vector of the base station $\boldsymbol{p}_{bs}$. Assuming no multipath and no obstruction, the DOA of the signal is the DOA of the LOS vector.
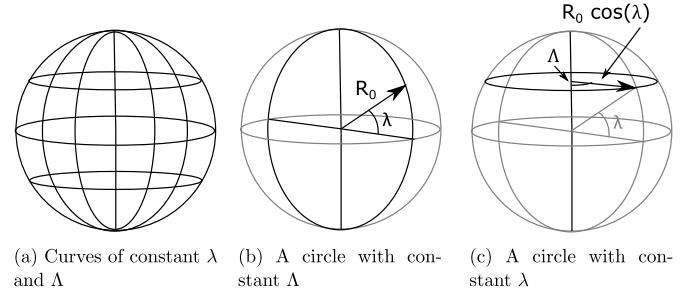

(a) Curves of constant λ and Λ

(b) A circle with constant Λ

(c) A circle with constant λ

Fig. 2. A spherical Earth of radius R_0, and its latitude λ and longitude Λ polar coordinate reference.

The array LOS measurement is based on DOA estimation, which uses the received signal phase shift estimates between sets of antennas. Examples of phase shift estimators are ESPRIT [30] and MUSIC [31]. In [22], both approaches provide similar results. Being the ESPRIT the simpler and less computationally intensive approach, we incorporate it in our proposed framework.

In [24], the antenna array in conjunction with the ESPRIT estimator is applied for attitude estimation. However, $\boldsymbol{d}_{NED}$, the LOS vector represented in S_{NED}, must be also measured. Such information can be obtained by a GPS receiver, which is commonly found in UAVs.

Assuming that both the UAV and the base station are equipped with GPS receivers, the difference between the positions of the UAV $\boldsymbol{p}_{UAV}$ and the base station $\boldsymbol{p}_{bs}$ (Fig. 1) in any Cartesian frame is the LOS vector:

$$\boldsymbol{d} = \boldsymbol{p}_{UAV} - \boldsymbol{p}_{bs}. \qquad (6)$$

The latitude, longitude and altitude (LLA) position of the base station is defined as, respectively, λ_{bs}, Λ_{gs}, and h_{bs}, and, similarly, the UAV LLA position is defined as λ_{UAV}, Λ_{UAV}, and h_{UAV}. The vector $\tilde{\boldsymbol{d}}_{NED}$ is the difference between the base and the plane positions in the S_{NED} frame, which is after normalized to $\boldsymbol{d}_{NED}$.

Fig. 2a shows the LLA coordinate system at the surface of a perfectly spherical Earth. Circles of constant longitude are concentric to the Earth's center, as shown in Fig. 2b, and have the same radius as Earth. Increasing λ is equivalent to a south–north movement. Circles of constant λ, except for $\lambda = 0$, are not concentric to the Earth's center, and their radii are equal to $R_0 \cos(\lambda)$, as shown in Fig. 2c. Increasing Λ is equivalent to a west-east movement.

Assuming that the UAV and the base station are close enough, and near the Earth's surface, the effects of the curvature of the Earth are negligible. The latitude and longitude differences between the UAV and ground station given by $\Delta_\lambda = \lambda_{UAV} - \lambda_{gs}$ and $\Delta_\Lambda = \Lambda_{UAV} - \Lambda_{gs}$ respectively, can be transformed to linear distances by calculating the length of the arc circles, and assuming that the arcs are almost straight lines [32]. Therefore, the three $\boldsymbol{d}_{NED}$ components are obtained by the two arcs and the altitude difference between the UAV and the ground station:

$$\tilde{d}_{\text{NED},x} = R_0 \cdot (\Delta_\lambda), \tag{7}$$

$$\tilde{d}_{\text{NED},y} = R_0 \cdot (\Delta_\Lambda) \cdot \cos(\frac{\lambda_{\text{UAV}} + \lambda_{\text{gs}}}{2}), \tag{8}$$

$$\tilde{d}_{\text{NED},z} = h_{\text{UAV}} - h_{\text{gs}}, \tag{9}$$

$$\boldsymbol{d}_{\text{NED}} = \tilde{\boldsymbol{d}}_{\text{NED}}/||\tilde{\boldsymbol{d}}_{\text{NED}}||, \tag{10}$$

where $R_0 = 6378138$ meters is the Earth radius.

If the plane and the base station are very far from each other, the Earth's curvature cannot be neglected. In this case, the distance between the base station and the UAV can be calculated using the S_{ECEF} frame which is detailed in [28,33,34].

The GPS measurements have uncertainty, which means that $\tilde{\boldsymbol{d}}_{\text{NED}}$ can be modeled as the sum of the true distance $\tilde{\boldsymbol{d}}_{\text{NED},0}$ and an error $\tilde{\boldsymbol{v}}_{\text{GPS}}$, i.e.:

$$\tilde{\boldsymbol{d}}_{\text{NED}} = \tilde{\boldsymbol{d}}_{\text{NED},0} + \tilde{\boldsymbol{v}}_{\text{GPS}}. \tag{11}$$

The vector $\tilde{\boldsymbol{v}}_{\text{GPS}}$ is the sum of the errors of the base station and UAV GPS receivers, and can be modeled by the covariance matrix $\boldsymbol{R}_{\text{GPS}}$.

The attitude estimator algorithms, however, use the normalized vector $\boldsymbol{d}_{\text{NED}}$ from (10) instead of $\tilde{\boldsymbol{v}}_{\text{GPS}}$. Since the normalization changes the scale of the measured vector, the noise vector is also re-scaled. Also, since the normalization process of the vector uses its own noise-corrupted components when calculating the norm, cross-correlations between components are inherently inserted. As shown in [35,36], the covariance matrix $\hat{\boldsymbol{R}}_{\text{d,GPS}}^*$ of the error vector $\boldsymbol{v}_{\text{GPS}}$ from the normalized vector $\boldsymbol{d}_{\text{NED}}$ can be calculated as:

$$\boldsymbol{R}_{\text{d,GPS}}^* = [\boldsymbol{d}_{\text{NED}}\times]^2 \boldsymbol{R}_{\text{GPS}}([\boldsymbol{d}_{\text{NED}}\times]^2)^{\text{T}}/||\tilde{\boldsymbol{d}}_{\text{NED}}||^2, \tag{12}$$

where $[\boldsymbol{a}\times]$ is the cross product matrix defined as

$$[\boldsymbol{a}]_\times = \begin{bmatrix} 0 & -a_3 & a_2 \\ a_3 & 0 & -a_1 \\ -a_2 & a_1 & 0 \end{bmatrix}. \tag{13}$$

Due to the unit-norm restriction, $\boldsymbol{R}_{\text{d,GPS}}^*$ is singular. As shown in [37] and explained by [35], an alternative non-singular covariance matrix $\boldsymbol{R}_{\text{d,GPS}}$ can be used without modifying the likelihood function:

$$\boldsymbol{R}_{\text{d,GPS}} = \boldsymbol{R}_{\text{d,GPS}}^* + 0.5 \cdot \boldsymbol{d}_{\text{NED}}\boldsymbol{d}_{\text{NED}}^{\text{T}} \cdot \text{trace}(\boldsymbol{R}_{\text{d,GPS}}^*). \tag{14}$$

The antenna array measurement vector $\boldsymbol{d}_b$ and GPS measurement vector $\boldsymbol{d}_{\text{NED}}$ can be related to each other by:

$$\boldsymbol{d}_{\text{b}} = \boldsymbol{D}_{\text{b}}^{\text{NED}} \cdot (\boldsymbol{d}_{\text{NED}} - \boldsymbol{v}_{\text{GPS}}) + \boldsymbol{v}_{\text{d}}, \tag{15}$$

where $\boldsymbol{v}_{\text{d}} \in \mathbb{R}^{3 \times 1}$ is an i.i.d. zero mean Gaussian random vector that represents LOS measurement error components described in S_{b}. Vectors $\boldsymbol{v}_{\text{GPS}}$ and $\boldsymbol{v}_{\text{d}}$ presented in (15) indicate that neither $\boldsymbol{d}_{\text{b}}$ nor $\boldsymbol{d}_{\text{NED}}$ are perfectly known, since both are affected by noise. The covariance matrix of $\boldsymbol{v}_{\text{d}}$ is defined as $\boldsymbol{R}_d$, and is derived in Section 5.2.

The attitude estimation algorithms compare the array measured $\boldsymbol{d}_b$ with the estimated $\hat{\boldsymbol{d}}_b$ obtained by rotating the GPS measurement vector $\boldsymbol{d}_{\text{NED}}$ using $\boldsymbol{D}_{\text{b}}^{\text{NED}}$. The noise covariance matrix $\boldsymbol{R}_{\text{AA+GPS}}$ of this difference, which includes both antenna array noise $\boldsymbol{v}_{\text{d}}$ and the rotated GPS noise $\boldsymbol{D}_{\text{b}}^{\text{NED}}\boldsymbol{v}_{\text{GPS}}$, must be provided to the Kalman filter, and is given by [8,35,36]

$$E[(\boldsymbol{d}_b - \hat{\boldsymbol{d}}_b)(\boldsymbol{d}_b - \hat{\boldsymbol{d}}_b)^{\text{T}}]$$
$$= \boldsymbol{R}_{\text{AA+GPS}} = \boldsymbol{R}_{\text{d}} + \boldsymbol{D}_{\text{b}}^{\text{NED}}\boldsymbol{R}_{\text{d,GPS}}[\boldsymbol{D}_{\text{b}}^{\text{NED}}]^{\text{T}}. \tag{16}$$

We describe the LOS measurement vector for some antenna array configurations in S_{ant} in Section 6. Equations (15) and (16) can be rearranged accordingly:
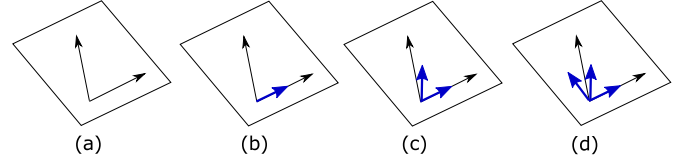

Fig. 3. The intermediate orthonormal basis S_{int} frame (in blue) generated by successive normalization and cross product calculations of two vectors (in black) that lie in a plane. (For interpretation of the references to color in this figure, the reader is referred to the web version of this article.)

$$\boldsymbol{d}_{\text{ant}} = \boldsymbol{D}_{\text{ant}}^{\text{NED}} \cdot (\boldsymbol{d}_{\text{NED}} - \boldsymbol{v}_{\text{GPS}}) + \boldsymbol{v}_{\text{d}}, \tag{17}$$

$$E[(\boldsymbol{d}_{\text{ant}} - \hat{\boldsymbol{d}}_{\text{ant}})(\boldsymbol{d}_{\text{ant}} - \hat{\boldsymbol{d}}_{\text{ant}})^{\text{T}}]$$
$$= \boldsymbol{R}_{\text{AA+GPS}} = \boldsymbol{R}_{\text{d}} + \boldsymbol{D}_{\text{ant}}^{\text{NED}}\boldsymbol{R}_{\text{d,GPS}}[\boldsymbol{D}_{\text{ant}}^{\text{NED}}]^{-1}. \tag{18}$$

4. Attitude estimation via TRIAD, QUEST and EKF

In order to obtain an initial estimate of the attitude, the two linear independent measurement vectors $\boldsymbol{d}_b$ and $\boldsymbol{m}_b$ from Section 3 are needed. Such initial estimate can be obtained by the TRIAD algorithm as explained in Subsection 4.1, or by the QUEST algorithm as explained in Subsection 4.2. Once there is an initial estimate of the attitude, we show in Subsection 4.3 that the EKF can be used to predict the attitude in the next time instant, and, afterwards, to fuse this predicted attitude with new sensor information. Note that the TRIAD or QUEST can also be used in standalone mode, i.e., without the EKF.

4.1. Attitude obtained by vector measurements via TRIAD

In this subsection, we present the relationship between the measurement vectors $\boldsymbol{d}_b$ and $\boldsymbol{m}_b$ obtained in Section 3 and the desired attitude defined by $\boldsymbol{D}_b^{\text{NED}}$, $\boldsymbol{q}$, or ψ, θ and ϕ.

The TRIAD algorithm [6,38] creates an intermediate orthonormal frame S_{int} by applying two non-orthonormal vectors. This process is shown in Fig. 3. In order to describe the three basis vectors of S_{int} in terms of S_{NED}, the vectors $\boldsymbol{d}_{\text{NED}}$ and $\boldsymbol{m}_{\text{NED}}$ are required, as shown in Fig. 3a.

Normalization and cross product operations are used to generate the orthonormal basis vectors $[\boldsymbol{x}_{\text{int}}]_{\text{NED}}$, $[\boldsymbol{y}_{\text{int}}]_{\text{NED}}$, and $[\boldsymbol{z}_{\text{int}}]_{\text{NED}}$, which are described by, respectively, (19), (20), (21) and depicted by, respectively, Figs. 3b, 3c, and 3d.

$$[\boldsymbol{x}_{\text{int}}]_{\text{NED}} = \boldsymbol{d}_{\text{NED}}, \tag{19}$$

$$[\boldsymbol{y}_{\text{int}}]_{\text{NED}} = \frac{\boldsymbol{d}_{\text{NED}} \times \boldsymbol{m}_{\text{NED}}}{||\boldsymbol{d}_{\text{NED}} \times \boldsymbol{m}_{\text{NED}}||}, \tag{20}$$

$$[\boldsymbol{z}_{\text{int}}]_{\text{NED}} = [\boldsymbol{x}_{\text{int}}]_{\text{NED}} \times [\boldsymbol{y}_{\text{int}}]_{\text{NED}}. \tag{21}$$

Using (3)

$$\boldsymbol{D}_{\text{NED}}^{\text{int}} = \begin{bmatrix} [\boldsymbol{x}_{\text{int}}]_{\text{NED}} & [\boldsymbol{y}_{\text{int}}]_{\text{NED}} & [\boldsymbol{z}_{\text{int}}]_{\text{NED}} \end{bmatrix}. \tag{22}$$

The same process is made with the array measured LOS vector $\boldsymbol{d}_b$ and the magnetometer-measured magnetic field vector $\boldsymbol{m}_b$ resulting in D_b^{int}

$$[\boldsymbol{x}_{\text{int}}]_{\text{b}} = \frac{\boldsymbol{d}_{\text{b}}}{||\boldsymbol{d}_{\text{b}}||}, \tag{23}$$

$$[\boldsymbol{y}_{\text{int}}]_{\text{b}} = \frac{\boldsymbol{d}_{\text{b}} \times \boldsymbol{m}_{\text{b}}}{||\boldsymbol{d}_{\text{b}} \times \boldsymbol{m}_{\text{b}}||}, \tag{24}$$

$$[\boldsymbol{z}_{\text{int}}]_{\text{b}} = [\boldsymbol{x}_{\text{int}}]_{\text{b}} \times [\boldsymbol{y}_{\text{int}}]_{\text{b}}. \tag{25}$$

$$\boldsymbol{D}_{\text{b}}^{\text{int}} = \begin{bmatrix} [\boldsymbol{x}_{\text{int}}]_{\text{b}} & [\boldsymbol{y}_{\text{int}}]_{\text{b}} & [\boldsymbol{z}_{\text{int}}]_{\text{b}} \end{bmatrix}. \tag{26}$$

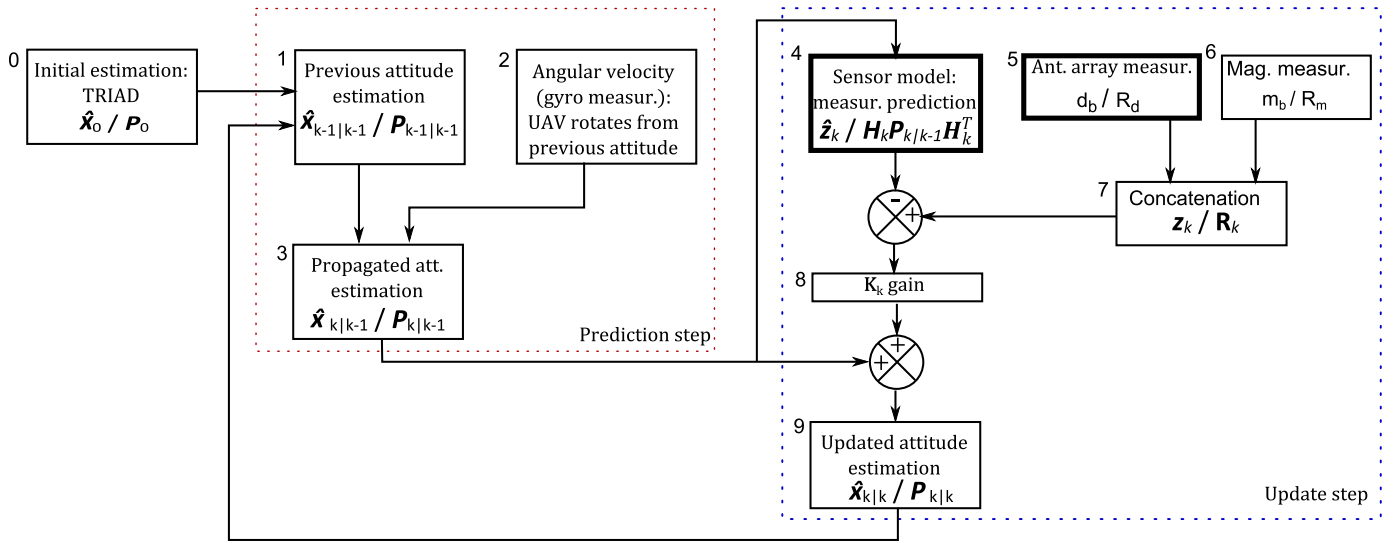The $\boldsymbol{D}_b^{\text{NED}}$ is the attitude of the UAV represented as an DCM, and is calculated as:

Fig. 4. EKF attitude estimator flowchart diagram. The EKF can be split in the prediction and update steps.

$$\boldsymbol{D}_{\mathrm{b}}^{\mathrm{NED}} = \boldsymbol{D}_{\mathrm{b}}^{\mathrm{int}} \left[\boldsymbol{D}_{\mathrm{NED}}^{\mathrm{int}} \right]^{\mathrm{T}}. \tag{27}$$

According to [39], the uncertainty related to the TRIAD estimation can be calculated as:

$$\boldsymbol{P}_{\mathrm{qq}} = \frac{\sigma_d^2 \boldsymbol{m}_b \boldsymbol{m}_b^{\mathrm{T}} + \sigma_m^2 \boldsymbol{d}_b \boldsymbol{d}_b^{\mathrm{T}}}{||\boldsymbol{d}_b \times \boldsymbol{m}_b||^2} + \sigma_d^2 [\boldsymbol{y}_{\mathrm{int}}]_{\mathrm{b}} [\boldsymbol{y}_{\mathrm{int}}]_{\mathrm{b}}^{\mathrm{T}}, \tag{28}$$

where $\boldsymbol{P}_{\mathrm{qq}}$ is a 3×3 error covariance matrix, in which the error is represented by small rotations around the $\boldsymbol{x}_b$, $\boldsymbol{y}_b$, and $\boldsymbol{z}_b$ body axes, and σ_d^2 and σ_m^2 represent the variance of the error in each element from $\boldsymbol{d}_b$ and $\boldsymbol{m}_b$. Equation (28) is not used in the TRIAD algorithm, but only in the proposed Kalman based attitude estimator. Note also that the magnitude of $||\boldsymbol{d}_{\mathrm{b}} \times \boldsymbol{m}_{\mathrm{b}}||$ decreases as $\boldsymbol{d}_{\mathrm{b}}$ and $\boldsymbol{m}_{\mathrm{b}}$ tend to align with each other and, as a consequence, the uncertainty $\boldsymbol{P}_{\mathrm{qq}}$ increases.

4.2. Attitude estimation using QUEST

The TRIAD algorithm presents basic limitations for possible applications. For instance, it is unable to use measurements of a third sensor to increase its performance. In addition, it does not take into account the relative uncertainty between sensors, weighting significantly more the first sensor in comparison with the second. On the other hand, the QUEST algorithm can tackle such limitations.

The QUEST algorithm [6] aims to find the attitude estimate $\boldsymbol{q}_{\mathrm{est}}$, in quaternion representation, that can best relate a set of at least two vectors on S_{NED} with their measured S_b counterpart, weighted by w_i scalar weights, which gives the relative confidence of the i-th sensor measurement related to the others. Here we define the weights w_d and w_m, from respectively, the antenna array and magnetometer, as the inverse of the trace of the respective covariance matrix.

$$w_d = 1/\operatorname{trace}(\boldsymbol{R}_d), \quad w_m = 1/\operatorname{trace}(\boldsymbol{R}_m). \tag{29}$$

The equations and full derivation of the QUEST algorithm can be found in [6].

4.3. Attitude estimation using extended Kalman filter

The Kalman filter can be used for any scenario involving dynamical systems and noisy measurements. In non-linear problems, its extended variant can be applied. In this subsection, we show an attitude estimation framework based on the Extended Kalman filter [7,8].

In contrast to QUEST and TRIAD, the EKF reuses the estimation from the previous time instant, which improves the quality and reduces the uncertainty of the actual estimation. This dynamical characteristic, that is estimated in a time instant and propagated to the next one, is described by the state variables $\boldsymbol{x}_k$ related to the k-th time instant. The propagation is based on angular rate measurements provided by gyro sensors. The EKF as well as QUEST can also incorporate measurements from extra sensors by weighting the uncertainty of each sensor. However, in contrast to QUEST, EKF can independently weight each vector component.

The EKF can also estimate the sensor errors as measurement bias including these errors as a component of the state of the system. Since the gyro sensor usually has a measurement bias, which is, for historical reasons, commonly named as gyro drift, this bias is also estimated by our EKF.

There are several quaternion-based Kalman attitude estimation schemes [7,8,40]. Due to the rotational quaternion unit-norm restriction, there are discussions about its effects on the performance of the EKF, and the best way to incorporate the unit norm restriction in the structure of the EKF. A common approach [3,7,40] is to reduce the estimated attitude quaternion error covariance from a 4×4 matrix to a 3×3 one. This work uses the *reduced representation of covariance matrix* Kalman based attitude estimation scheme [7].

In this approach, the estimated state vector $\hat{\boldsymbol{x}}$ contains seven elements: four from the attitude quaternion $\hat{\boldsymbol{q}}$ and three from the gyro drift $\hat{\boldsymbol{b}}$,

$$\hat{\boldsymbol{x}}_k = \begin{bmatrix} \hat{\boldsymbol{q}}_k \\ \hat{\boldsymbol{b}}_k \end{bmatrix}. \tag{30}$$

Fig. 4 depicts the EKF based attitude estimator split in prediction and update steps. From the Kalman filter perspective, one of the contributions of this work is to propose a sensor model and sensor measurement equations to the antenna array. Such contributions are depicted in Fig. 4 as Blocks 4 and 5.

In the prediction step, the algorithm starts in Block 1 from Fig. 4 using previous state estimation $\hat{\boldsymbol{x}}_{k-1|k-1}$ composed of attitude and gyro drift. The subscript $k-1|k-1$ stands for the $(k-1)$-th estimate obtained using the information from the $(k-1)$-th time instant. Except by the first iteration, the previous state estimation is provided by the previous update step of the Kalman filter

in Block 9. In the first iteration, the attitude estimation is originated from the TRIAD algorithm in Block 0, where the result must be converted from DCM to the quaternion representation, and the gyro drift estimate is assumed to be null. The estimated state has the uncertainty $P_{k-1|k-1}$ given by

$$P_{k-1|k-1} = \begin{bmatrix} P_{qq,k-1|k-1} & P_{qb,k-1|k-1} \\ P_{qb,k-1|k-1}^{\mathrm{T}} & P_{bb,k-1|k-1} \end{bmatrix}, \tag{31}$$

where the attitude uncertainty block $P_{qq,k-1|k-1}$ is initialized with the TRIAD estimation uncertainty (28), the gyro drift uncertainty block $P_{bb,k-1|k-1}$ is initialized based on the gyro calibration, and the cross correlation between the two uncertainties $P_{qb,k-1|k-1}$ is initialized null, since the initial attitude and drift estimates are obtained by non-correlated sources.

A dynamical model mathematically predicts the next state $\hat{x}_{k|k-1}$, i.e., the estimation of the state at k-th time instant using only information from the $(k-1)$-th time instant and from gyro measurements, as depicted in Block 2 from Fig. 4 in *prediction step*. Based on model and state uncertainty, the Kalman filter calculates the uncertainty of this prediction, as depicted in Block 3 from Fig. 4. This work uses the same dynamical model and Kalman filter equations as in [7], and they are omitted here for the sake of brevity.

As shown in [7], the source of the model (or process) noise $w_{d,k}$ includes the gyro noise and the slow changes of the gyro drift, and it increases the uncertainty of the predicted state. Here we model $w_{d,k}$ as a zero mean white Gaussian vector, defined by the covariance matrix $Q_{d,k}$

$$E[w_{d,j} \cdot w_{d,k}^{\mathrm{T}}] = Q_{d,k}\delta(j,k). \tag{32}$$

Here it is assumed that the gyro noise covariance Q_ω and the drift covariance Q_b are uncorrelated, i.e.

$$Q = \begin{bmatrix} Q_\omega & 0_{3x3} \\ 0_{3x3} & Q_b \end{bmatrix}. \tag{33}$$

In the update step, sensor measurements are used to increase the precision of the state estimate. The z_k in Block 7 is the vector concatenation of all measurements. In this work, z_k is the concatenation of the antenna array and magnetometer measurements, respectively d_{ant} and m_b, depicted respectively by Blocks 5 and 6 from Fig. 4.

$$z_k = \begin{bmatrix} m_b^{\mathrm{T}} & d_{ant}^{\mathrm{T}} \end{bmatrix}^T, \tag{34}$$

where d_{ant} is a more generic antenna array measurement than d_b, and its exact definition varies with the antenna configuration as detailed in Section 6.

The uncertainty of the measurement is described by the covariance matrix R_k in Block 7. In this work, R_k is composed of R_m and R_{AA+GPS}, respectively, from the magnetometer noise in Block 6 and from the sum of LOS measurement noise from the array in Block 5 and the GPS.

$$R = \begin{bmatrix} R_m & 0_{3 \times n} \\ 0_{n \times 3} & R_{AA+GPS} \end{bmatrix}. \tag{35}$$

R_m can be found in the sensor datasheet or via calibration process. R_{AA+GPS} depends on SNR and DOA of the signal, and on GPS noise, and can be calculated as shown in Subsections 3.2 and 5.2.

The EKF computes the prediction of z_k given by $\hat{z}_k$. Such prediction step illustrated in Block 4 in Fig. 4 uses the state estimation $\hat{x}_{k|k-1}$ from Block 3, since the measurements are related to the UAV attitude. The Kalman filter weights $\hat{z}_k$ and z_k in Block 8 based on the prediction and measurement uncertainties. Next this weighting process is used to minimize the uncertainty of the updated state $\hat{x}_{k|k}$ in Block 9.

The predicted measurement in Block 7 is:

$$\hat{z}_k = h(\hat{x}_{k|k-1}) \tag{36}$$

where $h(\cdot)$ denotes the concatenation of the known vectors m_{NED} and d_{NED}, rotated from S_{NED} to S_b using $\hat{D}_b^{NED}$ and to S_{ant} using $\hat{D}_{ant}^{NED}$. Note that $\hat{D}_b^{NED}$ and $\hat{D}_{ant}^{NED}$ are estimated DCMs calculated by using $\hat{x}_{k-1|k}$.

$$\hat{m}_b = \hat{D}_b^{NED}(\hat{x}_{k|k-1}) \cdot m_{NED}, \tag{37}$$

$$\hat{d}_{ant} = \hat{D}_{ant}^b \hat{D}_b^{NED}(\hat{x}_{k|k-1}) \cdot d_{NED}$$
$$= \hat{D}_{ant}^{NED}(\hat{x}_{k|k-1}) \cdot d_{NED}, \tag{38}$$

$$h(x_{k|k-1}) = \begin{bmatrix} \hat{m}_b^{\mathrm{T}} & \hat{d}_b^{\mathrm{T}} \end{bmatrix}^{\mathrm{T}}. \tag{39}$$

Since (36) is non-linear, in order to calculate the uncertainty of the $\hat{z}_k$ based on the $\hat{x}_{k|k-1}$ uncertainty, the non-linear model is linearized at $\hat{x}_{k|k-1}$, applying a Jacobian in $h(.)$:

$$H_k = \frac{\partial h(x)}{\partial x}\bigg|_{x_{k|k-1}} = \begin{bmatrix} H_{mb,k} & 0_{3 \times 3} \\ H_{dant,k} & 0_{n \times 3} \end{bmatrix}, \tag{40}$$

where $H_{mb,k} \in \mathbb{R}^{4 \times 3}$ and $H_{dant,k} \in \mathbb{R}^{4 \times n}$ are blocks of the Jacobian matrix relating, respectively, the three magnetometer and the n antenna array normalized phase shift measurements to the four attitude quaternion elements. Note that the two zero blocks indicate that the magnetometer and array measurements are unaffected by the three gyro drift elements present in the state vector.

In order to calculate the Jacobian blocks in a general fashion for any sensor measurement vectors on S_b, as the magnetometer ones, we refer to [8]. However, this is not the case with antenna array measurements, since they can be described in a more general frame S_{ant}.

As a contribution of the present work, we evaluate the case where the sensor is not aligned in S_b and/or the measurement vector components are not orthogonal to each other and/or it is redundantly measured with more than three vector components. Since the transformation $\hat{D}_{ant}^b$ from S_b to S_{ant} is a constant matrix, we can put it outside the Jacobian J(.) operation. This allows us to use the steps described in [8] to obtain $H_{db,k}$, which is the Jacobian related to the antenna array measurement assuming that it is measured on S_b, and after obtaining the desired $H_{dant,k}$

$$H_{dant,k} = J\left(\hat{D}_{ant}^b \hat{D}_b^{NED}(\hat{x}_{k|k-1}) \cdot d_{NED}\right)$$
$$= \hat{D}_{ant}^b \cdot J\left(\hat{D}_b^{NED}(\hat{x}_{k|k-1}) \cdot d_{NED}\right) \tag{41}$$
$$= \hat{D}_{ant}^b \cdot H_{db,k}$$

The measurement sensibility matrix H_k, together the measurement noise covariance matrix R_k, sensor measurement model $h(.)$ and the predicted state $x_{k|k-1}$ and its uncertainty $P_{k|k-1}$ are used to update the state estimation to $\hat{x}_{k|k}$ and to calculate its uncertainty $\bar{P}_{k|k}$. They are the output of the filter at k-th time instant. They are also the input of the next Kalman filter iteration at $k+1$-th time instant. As in the prediction step, the EKF update step equations are the same as from [7], and we omit them for the sake of simplicity.

5. Antenna array and LOS vector for attitude estimation

In Subsection 5.1, we overview the ESPRIT algorithm [30] in the context of attitude estimation, which is applied to estimate the phase shifts from the same source considering the sets of spatially distributed antennas. In Subsection 5.2, we propose a method to compute the phase shift error covariance in real time.
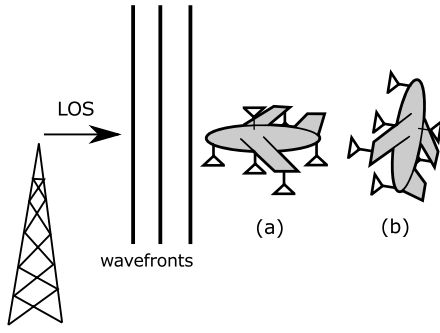
Fig. 5. A base station transmitting data to an antenna array in a UAV is illustrated in two distinct scenarios (a) and (b).
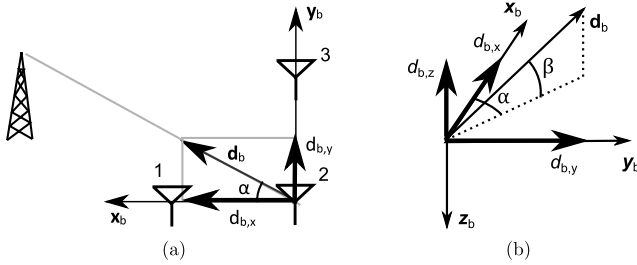

Fig. 6. The LOS vector d_b in S_b frame measured by pairs of antennas.

5.1. ESPRIT algorithm for attitude estimation

Consider a base station transmitting a signal to a UAV as depicted in Fig. 5. Since the signal travels with a finite speed from the transmitting antenna to each receiving antenna, each antenna of the UAV receives a differently delayed version of the same signal. Since the signal propagation speed and the inter-antenna spacing of the UAV are known, it is possible to find the DOA.

According to Fig. 5, variations in the attitude imply modifications of the antenna positions relative to the base station. The closest antenna from the antenna array to the base station receives the data first, i.e. the nose antenna in Fig. 5a and the left antenna in Fig. 5b.

In the literature, the DOA is usually defined as a set of two angles, elevation and azimuth. In [24], this pair of angles is denoted as a unitary vector described in polar coordinates. Therefore, another possible DOA representation is to use the Cartesian coordinates.

In Fig. 6a, a 2-D example shows an antenna configuration in which the Cartesian components $d_{b,x}$ and the $d_{b,y}$, or projections, of the unitary norm d_b are measured, and the equivalent polar coordinate α is shown. The 2–1 and 2–3 pairs of antennas measure, respectively, the $d_{b,x}$ and $d_{b,y}$ components. Assuming that the signal comes directly from the base station to the antenna array at the UAV, the Cartesian DOA represents a unitary vector d_b in S_b that points to the direction of the base station.

In Fig. 6b, three projections are measured by pairs of antennas, which can be used to reconstruct the full LOS vector. This unitary norm vector can be equivalently described by the two angles α and β.

A set of antennas arranged in a linear way gives only one angle of DOA, but this response is prone to ambiguity, since there are two possible angles for the same delay. A set arranged in a plane gives two angles also with ambiguity. However, a set arranged in a 3-D configuration gives the two angles without ambiguities. Next we relate the distribution of antennas with the d_b 3-D LOS vector components. For instance, in case of a linear configuration, we have only one component of d_b. In case of a planar configuration, there are two components of d_b, while in case of a 3-D configura-
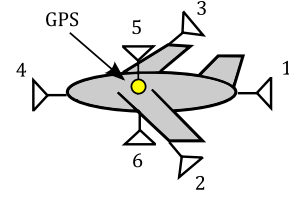
Fig. 7. Antenna positioning on the UAV. Note the pairs of antennas placed, respectively, along the x_b, y_b, z_b axis.
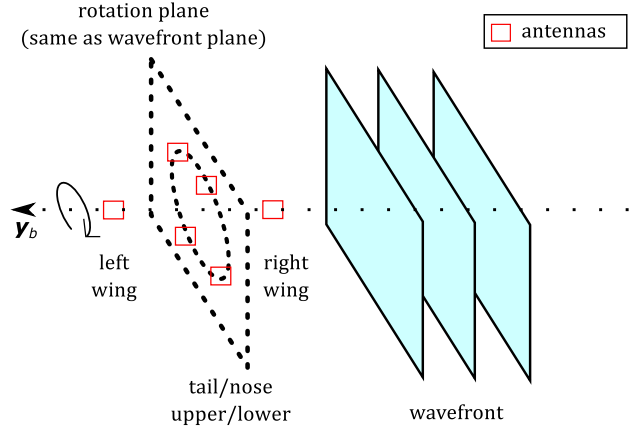

Fig. 8. Example of a rotation that does not affect antenna array measurements. The UAV is not shown in this figure, but only its antennas positions.

tion, there are three components of d_b. Since d_b has unitary norm, and if two of the three components are known, then the absolute value of the third one is also known. Note that the 3-D configuration removes the sign ambiguity of the planar one.

Fig. 7 shows an array configuration capable to measure all three d_b components or, equivalently, to obtain both DOA angles.

Note that the DOA alone cannot be used to fully determine the attitude, since there is no way to use only two angles, α and β, to estimate all three Euler angles, ψ, θ and ϕ. In Fig. 8, when an arbitrary magnitude rotation is applied on y_b axis, the wing antennas do not change positions. The tail, nose, upper, and lower antennas rotates within a plane parallel to the wavefront plane, which means that these four antennas are reached by the wavefront at the same time. The DOA, the phase shifts and time of arrival are constant, regardless of the rotation.

To obtain the DOA, or, equivalently, to obtain the 3 LOS vector components, the first step is to receive the data transmitted by the base station and record N samples gathered by each antenna. Applying the Hilbert transform, the narrowband signal changes to its analytical form, in which the time delay between two signals is transformed to a phase shift between two complex signals.

In this work, we adopt ESPRIT [30] to estimate the spatial frequencies. The ESPRIT algorithm is based on the shift invariance of the antenna array. By selecting K antenna equally spaced, the phase delay between antennas i and $i + 1$ is constant and equal to μ_{LOS}, for $1 \leq i \leq K - 1$.

The ESPRIT algorithm estimates the phase delay by the use of the eigenvalue decomposition (EVD) of the sample covariance matrix of the signal. The greatest d eigenvalues are related to the d signals, and the $K - d$ eigenvalues are related to noise. To estimate d, we refer to model order selection schemes in [41–43]. Since LOS vector has the strongest power, then the greatest eigenvalue also corresponds to it.

To measure this signal DOA, we choose pairs of antennas, i.e., $K = 2$. For each pair, the ESPRIT estimates only one element μ_{ij}, the phase shift between antennas i and j. We can normalize the obtained phase shifts using

$$\bar{\mu}_{ij} = \mu_{ij} \cdot \frac{\lambda}{2\pi \cdot L_{ij}}, \tag{42}$$

where λ is the wavelength of the signal and L_{ij} is the distance between antennas i and j. Note that L_{ij} normalizes the phase shift to 0 if there is no phase shift and 1 or -1 if it is the maximum physically allowed phase shift. In Section 3 it is explained how to use $\bar{\mu}_{ij}$ to obtain the $\boldsymbol{d}_b$. It is also worth noting that, in this work, we are not interested in α and β, but in $d_{b,i}$ components. This explains why there is no arcsin in (42), although it is the case in DOA estimator algorithms. To be best of our knowledge, the normalization step to obtain a Cartesian coordinate instead of arcsin for a polar coordinate is a minor contribution of this paper.

5.2. Phase shift error covariance

As important as estimating the phase shift is to know how good this estimation is, since the Kalman filter and QUEST approaches need both information in real time. Here we present, as contribution, the noise covariance calculation of the normalized phase shift measurement, based on the phase shift mean squared error calculation from [26].

The quality of the estimated phase shift $\hat{\mu}_{ij}$ can be described by its error covariance $R_{\hat{\mu}_{ij}}$ as a function of the true (and unknown) phase shift μ_{ij}:

$$R_{\hat{\mu}_{ij}} = E[(\mu_{ij} - \hat{\mu}_{ij})^2]. \tag{43}$$

We assume that $\boldsymbol{V}$ from the received signal $\boldsymbol{X}$ is a circularly symmetric white noise, i.e. its covariance $\boldsymbol{R}_V$ can be written as:

$$\boldsymbol{R}_V = \sigma_n^2 \cdot \boldsymbol{I}_K. \tag{44}$$

Since the ESPRIT algorithm is capable to obtain an estimation of the signal subspace of the received transmission, i.e., it can separate the signal from the noise, we can reconstruct an estimation of the noiseless signal. Subtracting the estimated noiseless signal from the received signal provides an estimate of the noise. Calculating this noise covariance it is obtained, assuming a pair of antennas, a 2×2 real matrix $\hat{\boldsymbol{R}}_V$, containing the variance of each antenna noise and the cross-covariance between each antenna noise. Assuming that $\hat{\boldsymbol{R}}_V$ has approximately the assumed structure described in (44), an estimate of σ_n^2 can be obtained by:

$$\hat{\sigma}_n^2 = \text{mean}(\text{diag}(\hat{\boldsymbol{R}}_V)). \tag{45}$$

Under the circular symmetric white noise assumption, the $R_{\hat{\mu}_{ij}}$ can be calculated as explained on the Appendix C from [26], which is what is done in this work. $R_{\hat{\mu}_{ij}}$ can also be calculated, in a more sophisticated fashion, without this circular symmetric white noise assumption, as explained in [26]. Both variants can be used in our framework.

As shown in (42), this work uses a normalized phase shift. The Kalman filter needs the error covariance of this normalized estimate, which can be calculated by

$$E[\Delta \bar{\mu}_{ij}^2] = R_{d_{ij}} = \left(\frac{\lambda}{2\pi \cdot L_{ij}}\right)^2 \cdot R_{\hat{\mu}_{ij}}. \tag{46}$$

Note that $R_{d_{ij}}$ is inversely proportional to the square of L_{ij}. Therefore, the farther are the consecutive antennas, the lower is the covariance error. Nevertheless, the antennas must not be farther than $\lambda/2$, i.e., half the wavelength of the signal due to the spatial aliasing. Note that this normalization step is different from the $\boldsymbol{d}_{\text{NED}}$ normalization in (10), since here the normalization scale factor L_{ij} is constant, assumed to be perfectly known and independent from the antenna array measurement or its error. This holds even when using three pairs of antennas to measure a unit-norm

vector, as in (49). Hence, the covariance calculation in (46) or in (49) is simpler and does not include cross-correlation factors as in (12).

6. Improving LOS vector by exploiting antenna array design

In Section 5, the normalized phase shift $\bar{\mu}_i$ of some i-th pair of antennas is calculated. The TRIAD algorithm needs the $\boldsymbol{d}_b$ LOS vector containing all 3 vector components as input.

The Kalman filter has a weaker requirement, i.e. it only needs a relationship between the normalized phase shifts and the GPS-obtained LOS vector that includes some information about S_b and S_{NED}. Equation (15) can be relaxed to the broader version as follows

$$\boldsymbol{d}_{\text{ant}} = \tilde{\boldsymbol{D}}_{\text{ant}}^b \boldsymbol{D}_b^{\text{NED}} \cdot \boldsymbol{d}_{\text{NED}} = \tilde{\boldsymbol{D}}_{\text{ant}}^b \boldsymbol{d}_b \tag{47}$$

where $\boldsymbol{d}_{\text{ant}}$ is a vector made of N stacked normalized phase shifts measurements, and can be understood as a vector measured in some S_{ant} antenna coordinate frame. $\tilde{\boldsymbol{D}}_{\text{ant}}^b$ is a $\mathbb{R}^{N,3}$ linear transformation matrix that changes $\boldsymbol{d}_b$ in the N phase-shifts. Note that, depending on the antenna configuration, the matrix $\tilde{\boldsymbol{D}}_{\text{ant}}^b$ is not a DCM.

The Kalman filter also needs the error covariance from the normalized phase shifts as shown in (35). As a contribution of this work, we find ways to provide the required information $\boldsymbol{d}_b$, $\boldsymbol{d}_{\text{ant}}$, and $\tilde{\boldsymbol{D}}_{\text{ant}}^b$ in several antenna configurations. The suggested configurations, and the provided analysis for each one, assume that the reception and noise are not affected by the antenna position, i.e., it is the relative antenna position design that it is evaluated. However, the designs can be configurable to treat problems in practical scenarios, such as the disturbance caused by the approximation between the antenna and the noisy engine.

As depicted in Fig. 6, a pair of antennas measures the projection of $\boldsymbol{d}_b$ in the normalized vector connecting the first antenna to the second one. In Subsections 6.1 and 6.2, the array is designed to have pairs of antennas physically displaced in each of the three S_b axis, which directly provides the three S_b components of $\boldsymbol{d}_b$. In Subsections 6.3 and 6.4, the antenna positioning restriction is relaxed, at the cost of extra computational complexity and, in Subsection 6.4, of loss of precision. In Subsection 6.5, it is shown that more ingenious choices of pairs of antennas in previous designs can provide better results in some scenarios. Finally, in Subsection 6.6, we propose to use more than three pairs of antennas in low SNR regimes.

6.1. Previous cross-shaped six antenna array

In [24], it is studied the antenna configuration shown in Fig. 7. In this scenario, the UAV is equipped with six antennas with a pair in each UAV axis. This configuration is also symmetric relative to the GPS, i.e. the GPS is at the center of the UAV, and antennas from same pair are equally spaced with respect to the GPS.

In such straightforward configuration, each pair provides one of the three $\boldsymbol{d}_b$ components. For instance, the normalized phase shift from the antenna pair 1–4 on x axis provides the $d_{b,x}$ component from $\boldsymbol{d}_b$. Note that the vector that starts at antenna 1 and points to antenna 4 has the same direction and sign as $\boldsymbol{x}_b$, whereas the sequence 4–1 has the opposite sign. Defining $\bar{\mu}_{i,j}$ as the normalized phase shift between antennas i and j, $\boldsymbol{d}_b$ can be written as

$$\boldsymbol{d}_b = \begin{bmatrix} \bar{\mu}_{1,3} & \bar{\mu}_{2,4} & \bar{\mu}_{5,6} \end{bmatrix}^T. \tag{48}$$

The estimated normalized phase shift error covariance matrix $\boldsymbol{R}_d$ is equal to

$$\boldsymbol{R}_d = \text{diag}(\begin{bmatrix} R_{d_{1,3}} & R_{d_{2,4}} & R_{d_{5,6}} \end{bmatrix}). \tag{49}$$
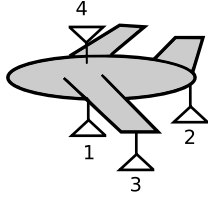
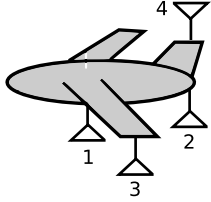**Fig. 9.** Four antenna array configuration.

Fig. 10. Alternative four antennas configuration.

In this configuration, the Kalman filter uses the measurement in the same way as the TRIAD algorithm, i.e., $\boldsymbol{d}_{\text{ant}} = \boldsymbol{d}_b$ and $\tilde{\boldsymbol{D}}_{\text{ant}}^b = \boldsymbol{I}_3$.

6.2. Proposed four-antenna array aligned with body axis

Aiming to reduce the hardware cost, here we propose to reduce the number of antennas obtaining similar results. As shown along this subsection, the minimum amount of antennas to measure all components of a 3D LOS vector is four. Each pair of antennas creates a basis vector of the frame S_{ant}. If there are only three antennas, they certainly are contained on a single plane, and any combination of pairs of antennas generates a basis in this plane. Four antennas can map a 3-D space as shown in Fig. 9. In this configuration, the pairs of antennas are aligned with the S_b axis in a way that the S_b and S_{ant} frames are exactly the same.

In contrast to the six antenna array configuration in Fig. 7, the four antenna array configuration in Fig. 9 needs to repeat the antennas to obtain $\boldsymbol{d}_b$, since three pairs of antennas are necessary. Choosing pair of antennas that generates vectors that are parallel and with the same sign as respectively $\boldsymbol{x}_b$, $\boldsymbol{y}_b$, and $\boldsymbol{z}_b$, $\boldsymbol{d}_b$ is obtained as:

$$\boldsymbol{d}_b = \begin{bmatrix} \bar{\mu}_{2,1} & \bar{\mu}_{3,1} & \bar{\mu}_{4,1} \end{bmatrix}^{\text{T}}. \tag{50}$$

In this four antenna array configuration, the antenna one is used in all three measurements. If for some reason this antenna measurement is noisier than the other antenna measurements, this extra noise will be present in all three components of $\boldsymbol{d}_b$. Furthermore, there is a cross-correlation $R_{d_{i,1;j,1}}$ between the measurements from the pairs $i,1$ and $j,1$:

$$\boldsymbol{R}_d = \begin{bmatrix} R_{d_{2,1}} & R_{d_{2,1;3,1}} & R_{d_{2,1;4,1}} \\ R_{d_{2,1;3,1}} & R_{d_{3,1}} & R_{d_{3,1;4,1}} \\ R_{d_{2,1;4,1}} & R_{d_{3,1;4,1}} & R_{d_{4,1}} \end{bmatrix}. \tag{51}$$

For the sake of simplicity, we assume that the cross correlations in (51) are equal to zero.

An alternative configuration that uses each antenna no more than twice is shown in Fig. 10. This is an example showing that the pairs of antennas do not need to have a common origin, and other similar examples can be obtained by the use of the same idea. In this case, $\boldsymbol{d}_b$ is calculated as:

$$\boldsymbol{d}_b = \begin{bmatrix} \bar{\mu}_{2,1} & \bar{\mu}_{3,1} & \bar{\mu}_{4,2} \end{bmatrix}^{\text{T}}. \tag{52}$$

The structure of $\boldsymbol{R}_d$ is shown in (53). Note that there is no cross-correlation between $\bar{\mu}_{3,1}$ $\bar{\mu}_{4,2}$, since they do not share antennas. Here we assume that all the cross correlations are zero.
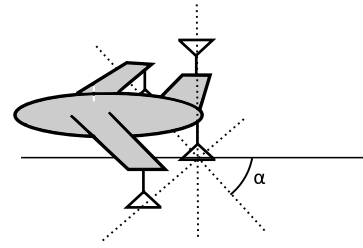

Fig. 11. An example where the antennas make an orthogonal coordinate system S_b (shown by the dashed lines) that is not aligned with S_b, where x_b is shown as a continuous line.

$$\boldsymbol{R}_d = \begin{bmatrix} R_{d_{2,1}} & R_{d_{2,1;3,1}} & R_{d_{2,1;4,2}} \\ R_{d_{2,1;3,1}} & R_{d_{3,1}} & 0 \\ R_{d_{2,1;4,2}} & 0 & R_{d_{4,2}} \end{bmatrix}. \tag{53}$$

Due to the simplicity of the configurations in Fig. 9 and in Fig. 10, the Kalman filter uses the measurement in the same way as the TRIAD algorithm, i.e., $\boldsymbol{d}_{\text{ant}} = \boldsymbol{d}_b$ and $\tilde{\boldsymbol{D}}_{\text{ant}}^b = \boldsymbol{I}_3$.

6.3. Proposed four-antenna array for any orthogonal configuration

A more realistic assumption is that the antennas are positioned in an arbitrary fashion in order to optimize the communication link instead of attitude estimation.

One special case is that the four antenna array still generates an orthogonal set of basis vectors when defining one of the antennas as an origin and the vectors as the normalized vectors connecting the origin antenna to the other three antennas. Fig. 11 shows an example where a misalignment is caused by a single rotation α around the z_b axis in Fig. 9.

In this special case, this set of vectors defines a new orthogonal coordinate system S_{ant}. This new frame can be related to S_b in the same way we relate S_b to S_{NED}. For instance, we can use a DCM $\boldsymbol{D}_{\text{ant}}^b$ to rotate a vector from S_b to S_{ant}, i.e.

$$\boldsymbol{d}_{\text{ant}} = \boldsymbol{D}_{\text{ant}}^b \boldsymbol{D}_b^{\text{NED}} \cdot \boldsymbol{d}_{\text{NED}} = \boldsymbol{D}_{\text{ant}}^b \boldsymbol{d}_b. \tag{54}$$

Since the antennas are in a fixed position related to the UAV, $\boldsymbol{D}_{\text{ant}}^b$ is constant, and can be calculated off-line. Also, being a DCM, its inverse is equal to its transpose:

$$\boldsymbol{D}_b^{\text{ant}} = (\boldsymbol{D}_{\text{ant}}^b)^{\text{T}}. \tag{55}$$

In the example, the measurement vector $\boldsymbol{d}_{\text{ant}}$, $\boldsymbol{D}_{\text{ant}}^b$ and $\boldsymbol{d}_b$ are:

$$\boldsymbol{d}_b = \begin{bmatrix} \bar{\mu}_{2,1} & \bar{\mu}_{3,1} & \bar{\mu}_{4,2} \end{bmatrix}^{\text{T}}, \tag{56}$$

$$\boldsymbol{D}_{\text{ant}}^b = \begin{bmatrix} \cos(\alpha) & \sin(\alpha) & 0 \\ -\sin(\alpha) & \cos(\alpha) & 0 \\ 0 & 0 & 1 \end{bmatrix}, \tag{57}$$

$$\boldsymbol{d}_b = \boldsymbol{D}_b^{\text{ant}} \boldsymbol{d}_{\text{ant}}. \tag{58}$$

Note that the measurement error covariance $\boldsymbol{R}_d$ is the same as (53). In this case, $\tilde{\boldsymbol{D}}_{\text{ant}}^b$ from the Kalman filter approach is equal to $\boldsymbol{D}_{\text{ant}}^b$.

6.4. Proposed arbitrary four-antenna array configuration

Here we relax the assumption that the four antenna array is aligned with the body axis and provides an orthogonal basis. The only restriction is that the basis formed by the antennas maps a 3D space. In other words, the four antenna positions must not all lie on a single plane, or line or point.

According to (3), it is possible to find a transformation matrix from S_b to S_{ant} by simply describing the basis vector from S_{ant} in
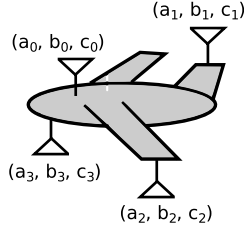
Fig. 12. An example where the antenna positions do not follow any pattern. Each antenna has a coordinate (a_i, b_i, c_i) at S_b.

S_b frame. Defining one antenna as origin, the normalized vector connecting the origin with the other antennas can be seen as basis. Note that the basis vectors are simply the normalized relative position between each antenna and the origin antenna.

As shown in Fig. 12, each antenna has one position described using the S_b frame. Assuming that antenna 0 is the origin, the three relative positions $\Delta \boldsymbol{p}_{1,i}$ are equal to:

$$\Delta \boldsymbol{p}_i = \begin{bmatrix} a_i - a_0 & b_i - b_0 & c_i - c_0 \end{bmatrix}^T. \tag{59}$$

The normalized $\Delta \boldsymbol{p}_i$ is used to find the transformation matrix $\tilde{\boldsymbol{D}}_{\mathrm{ant}}^{\mathrm{b}}$:

$$\tilde{\boldsymbol{D}}_{\mathrm{ant}}^{\mathrm{b}} = \begin{bmatrix} \dfrac{\Delta \boldsymbol{p}_1}{||\Delta \boldsymbol{p}_1||} & \dfrac{\Delta \boldsymbol{p}_2}{||\Delta \boldsymbol{p}_2||} & \dfrac{\Delta \boldsymbol{p}_3}{||\Delta \boldsymbol{p}_3||} \end{bmatrix}^T. \tag{60}$$

Since the antennas are in a fixed position with respect to the UAV, $\tilde{\boldsymbol{D}}_{\mathrm{ant}}^{\mathrm{b}}$ is constant, and can be calculated off-line. Since $\tilde{\boldsymbol{D}}_{\mathrm{ant}}^{\mathrm{b}}$ is not a DCM, its inverse is not equal to its transpose. In order that $\tilde{\boldsymbol{D}}_{\mathrm{ant}}^{\mathrm{b}}$ be invertible, the three basis vectors must be linear independent. Therefore, in this configuration, the four antennas cannot lie on a single plane.

$$\tilde{\boldsymbol{D}}_{\mathrm{b}}^{\mathrm{ant}} = (\tilde{\boldsymbol{D}}_{\mathrm{ant}}^{\mathrm{b}})^{-1}. \tag{61}$$

In Fig. 12, the measurement vector $\boldsymbol{d}_{\mathrm{ant}}$, its representation in the S_b frame $\boldsymbol{d}_{\mathrm{b}}$, and its error covariance matrix $\boldsymbol{R}_d$ are:

$$\boldsymbol{d}_{\mathrm{ant}} = \begin{bmatrix} \bar{\mu}_{0,1} & \bar{\mu}_{0,2} & \bar{\mu}_{0,3} \end{bmatrix}^T, \tag{62}$$

$$\boldsymbol{d}_{\mathrm{b}} = \tilde{\boldsymbol{D}}_{\mathrm{b}}^{\mathrm{ant}} \boldsymbol{d}_{\mathrm{ant}}, \tag{63}$$

$$\boldsymbol{R}_d = \begin{bmatrix} R_{d_{0,1}} & R_{d_{0,1;0,2}} & R_{d_{0,1;0,3}} \\ R_{d_{0,1;0,2}} & R_{d_{0,2}} & R_{d_{0,2;0,3}} \\ R_{d_{0,1;0,3}} & R_{d_{0,2;0,3}} & R_{d_{0,3}} \end{bmatrix}. \tag{64}$$

To analyze the antenna positioning effect in the estimation performance, we use an unnormalized matrix transformation $\check{\boldsymbol{D}}_{\mathrm{ant}}^{\mathrm{b}}$ instead of $\tilde{\boldsymbol{D}}_{\mathrm{ant}}^{\mathrm{b}}$:

$$\check{\boldsymbol{D}}_{\mathrm{ant}}^{\mathrm{b}} = \begin{bmatrix} \Delta \boldsymbol{p}_1 & \Delta \boldsymbol{p}_2 & \Delta \boldsymbol{p}_3 \end{bmatrix}^T. \tag{65}$$

When using $\check{\boldsymbol{D}}_{\mathrm{ant}}^{\mathrm{b}}$, all related algorithms must be adjusted. We use the phase shifts instead of the normalized phase shifts as a measurement vector. In addition, the noise covariance is calculated as $R_{\hat{\mu}_{ij}}$ from [26] instead of (46), i.e., the unnormalized covariance is used instead of the normalized one. The inverse of the unnormalized $\check{\boldsymbol{D}}_{\mathrm{ant}}^{\mathrm{b}}$ normalizes in S_b the unnormalized measurement vector in S_{ant}:

$$\boldsymbol{d}_{\mathrm{b}} = (\check{\boldsymbol{D}}_{\mathrm{ant}}^{\mathrm{b}})^{-1} \check{\boldsymbol{d}}_{\mathrm{ant}}. \tag{66}$$

Since $\check{\boldsymbol{D}}_{\mathrm{b}}^{\mathrm{ant}} = (\check{\boldsymbol{D}}_{\mathrm{ant}}^{\mathrm{b}})^{-1}$ transforms not only the vector, but also the noise, this matrix can be used to measure how much the phase shift uncertainty is magnified or reduced, helping to choose the combination of antenna pairs for which the magnification of noise

is minimized. Since evaluating the full matrix is not easy, then here we propose a scalar parameter. Assuming that all unnormalized phase shifts noise have the same magnitude, we can define a magnifying factor f:

$$f = \det(\check{\boldsymbol{D}}_{\mathrm{b}}^{\mathrm{ant}}) = \frac{1}{\det(\check{\boldsymbol{D}}_{\mathrm{ant}}^{\mathrm{b}})}, \tag{67}$$

where the smaller is the f, the better is the choice of the pairs of antennas. This idea is based on the Covariance Intersection (CI) algorithm [44], where the determinants of a set of covariance matrices are used to decide which one provides the lowest noise. The determinant is the product of the matrix eigenvalues describing their overall effect. This criterion has a drawback of not describing the effect of each eigenvalue individually.

If the distance between pairs of antennas is constant, it can be seen from (67) that the uncertainty grows when the pairs of antennas tend to become linearly dependent. Such increased uncertainty comes from the fact that matrices with linearly dependent columns provide a null determinant.

6.5. Proposed selection of unusual phase shifts in an arbitrary four-antenna array configuration

As shown in Subsection 6.3, the antenna configuration from Fig. 10 is more robust than Fig. 9, since the last one relies heavily in a single antenna. Here it is discussed how this extra robustness can be obtained by software from configurations according to Fig. 9 without changing the antenna position.

In Subsection 6.4, it is explained how to use sets of phase shifts from antennas aligned in any direction. This idea can be used in any configuration, even in orthogonal ones. Then we choose pairs of antennas that meet some desired criteria, instead of being limited to choosing pairs that are aligned to some axis or orthogonal to another pair. For example, in Fig. 9, we can use a set of phase shifts that does not include the same antenna more than twice:

$$\boldsymbol{d}_{\mathrm{ant}} = \begin{bmatrix} \bar{\mu}_{2,1} & \bar{\mu}_{3,2} & \bar{\mu}_{4,2} \end{bmatrix}^T. \tag{68}$$

In this case, the covariance matrix from $\boldsymbol{d}_{\mathrm{ant}}$, $\boldsymbol{R}_d$, is equal to (53). In the same way as in Fig. 12, $\tilde{\boldsymbol{D}}_{\mathrm{ant}}^{\mathrm{b}}$ and $\boldsymbol{d}_{\mathrm{b}}$ can be calculated by (60) and (63). Equation (67) can be used to choose the best combination of antenna pairs, in which the measurement noise is smaller.

6.6. Inclusion of additional phase shifts in an arbitrary four-antenna array

Up to this subsection, we are assuming that we can use only three phase shifts to obtain $\boldsymbol{d}_{\mathrm{ant}}$, $\tilde{\boldsymbol{D}}_{\mathrm{ant}}^{\mathrm{b}}$ and $\boldsymbol{d}_{\mathrm{b}}$. If there is no noise, this is true, as extra phase shifts can be seen as vectors that are linear dependent from the three basis vectors bringing no new information. However, being the phase shift imperfect measurements, using extra phase shifts can reduce the uncertainty.

The Kalman filter can process more, or less, than three measurements with no special modification. It is necessary only to obtain the relationship between the LOS vector in S_{NED} and all the measurements, i.e., we need to find the linear transformation that, when applied in d_{NED}, results in d_{ant}, the concatenation of all normalized measured phase shifts. This relationship is described in (47). For n normalized phase shifts measurements, the $\tilde{\boldsymbol{D}}_{\mathrm{ant}}^{\mathrm{b}}$ $R^{n \times 3}$ matrix can be obtained in a similar way from (60):

$$\tilde{\boldsymbol{D}}_{\mathrm{ant}}^{\mathrm{b}} = \begin{bmatrix} \dfrac{\Delta \boldsymbol{p}_1}{||\Delta \boldsymbol{p}_1||} & \cdots & \dfrac{\Delta \boldsymbol{p}_n}{||\Delta \boldsymbol{p}_n||} \end{bmatrix}^T, \tag{69}$$

where $\Delta \boldsymbol{p}_i$ is the vectorial distance between the i-th pair of two arbitrary antennas j and k, $j \neq k$:

Table 1

Sensors specifications for each one of the three axis.

Sensor	Measurement bias	Noise covariance
GPS	0	100 m^2
Magnetometer	0 nmf[*]	$1.2 \cdot 10^{-4}$ nmf^2
Gyro	$9.7 \cdot 10^{-3}$ rad/s	$1.2 \cdot 10^{-2}$ (rad/s)^2

[*] A unit in which the local magnetic field has unitary norm.

$$\Delta \boldsymbol{p}_i = \begin{bmatrix} a_j - a_k & b_j - b_k & c_j - c_k \end{bmatrix}^{\mathrm{T}}. \tag{70}$$

If we want to use these extra phase shift estimates in the TRIAD or QUEST algorithms, we must solve $\boldsymbol{d}_b$ from $\boldsymbol{d}_{\mathrm{ant}}$ using (47). Since we have three parameters to be determined and have n equations (rows), this is an over-determined system. Moreover, the covariance of the estimation error of each component of $\boldsymbol{d}_{\mathrm{ant}}$ is not equal. Therefore, the best estimate of $\boldsymbol{d}_b$ can be obtained by the generalized least squares method:

$$\boldsymbol{d}_b = [(\tilde{\boldsymbol{D}}_{\mathrm{ant}}^b)^{\mathrm{T}} \boldsymbol{R}_d^{-1} \tilde{\boldsymbol{D}}_{\mathrm{ant}}^b]^{-1} \tilde{\boldsymbol{D}}_{\mathrm{ant}}^b \boldsymbol{R}_d^{-1} \boldsymbol{d}_{\mathrm{ant}} \tag{71}$$

Since it is possible to use more than three phase shift estimates, one can wrongly assume that the best is to use all the phase shifts, i.e., all distinct antenna pair combinations. In the four antenna case, for example, this means six phase shifts. However, this is not true. The extra phase shifts have correlations with the initial ones, since each new measurement shares one antenna from the pair used in some previous measurement. In addition, when measuring unitary norm vector projections, there is the norm restriction, which is a non-linear characteristic. Neither the EKF, nor the generalized least squares method, works perfectly well with non-linearities, and each new measurement strengthens the non-linear effect.

From simulations, we obtained best results when following these empirical rules:

- Choose three pairs of antennas that form an orthogonal basis, or at least basis vectors that have low projections between each other, i.e., vectors that provide the highest value of f in (67).
- Choose one to three extra pairs. Each pair relates a basis vector to another. Example: choose one antenna from the first basis and another one from the second basis, then one from the second and another one from the third, then another one from the third and another one from the first.
- Whenever possible, try to reduce the number of repeated antennas.

7. Simulation results

All the developed algorithms are evaluated by simulation using the Simulink graphical programming environment from MATLAB R2013b. The simulation consists in a UAV flying about 1000 m away from a base station. For each scenario, 500 Monte Carlo trials are used to produce the mean performance.

The UAV is equipped with a GPS receiver, magnetometer and gyro sensors. All sensor measurements are corrupted by a zero mean white Gaussian noise. The gyro is corrupted also by drift, i.e. a biased measurement error, and also corrupted by the Earth rotation, which is $2\pi/(24\ \mathrm{h}) = 73 \cdot 10^{-6}$ rad/s. All sensors provide data at 100 Hz. Table 1 summarizes the sensors specifications.

The UAV also carries an antenna array containing four or six antennas according to the configurations described in Section 6. Tables 2 to 4 summarize the evaluated antenna configurations.

Six physical antenna positioning are evaluated. In configuration 1), six antenna array from Fig. 7 is considered. In 2), four antenna array orthogonal configuration from Fig. 9 is considered. 3) four

Table 2

Antenna positions in several 4-antennas configurations related to the position of the antenna 1, described in S_b.[a]

Cfg.	Antenna 2 (x, y, z)	Antenna 3 (x, y, z)	Antenna 4 (x, y, z)
2	$(-L_x, 0, 0)$	$(0, -L_y, 0)$	$(0, 0, -L_z)$
3	$(-L_x, 0, 0)$	$(0, -L_y, 0)$	$(-L_x, 0, -L_z)$
4[b]	$-L_x(\mathrm{c}(\pi/4), \mathrm{s}(\pi/4), 0)$	$-L_y(-\mathrm{s}(\pi/4), \mathrm{c}(\pi/4), 0)$	$(0, 0, -L_z)$
5[c]	$-L_x(\mathrm{c}(\alpha_1), \mathrm{s}(\alpha_1), 0)$	$-L_y(-\mathrm{s}(\alpha_2), \mathrm{c}(\alpha_2), 0)$	$(0, 0, -L_z \mathrm{c}(\beta))$

[a] $L_x = 0.76$ m, $L_y = 1.2$ m, $L_z = 0.3$ m, unless otherwise stated.

[b] $\mathrm{c}(\cdot)$ and $\mathrm{s}(\cdot)$ means, respectively, the cosine and sine functions, written in a compact way.

[c] $\alpha_1 = \pi/4 + \beta/2$, $\alpha_2 = \pi/4 - \beta/2$, β changes in each scenario.
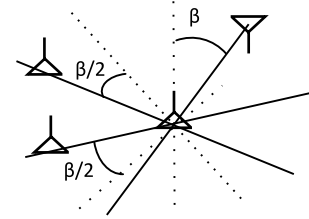
Fig. 13. Non-orthogonal configuration 5.

Table 3

Pairs of antennas that are source of phase shift estimations in four and six antenna array configurations.

Configuration	Pairs of antennas
a	2–1, 3–1, 4–1
b	2–1, 3–1, 4–2
c	1–4, 2–3, 5–6
d	1–4, 2–3, 5–6, 1–2, 3–5, 4–6

antenna array orthogonal alternative configuration from Fig. 10 is considered. In 4), four antenna array orthogonal, rotated from S_b, from Fig. 11, is considered. In 5), four antenna array in non-orthogonal configuration, as described by Fig. 13, with a varying angle β, is considered. Configuration 5) from Fig. 13 starts from rotated configuration 4), shown as dotted lines. Varying the angle β, one antenna stays at the same place, 2 antennas move within the horizontal plane, approaching each other, and the last antenna approaches the horizontal plane. The distance between the moving antennas and the fixed antenna is constant. For $\beta = 90°$, all antennas stay in the same line. Table 2 shows the physical antenna positioning for the four antenna array configurations 2) to 5).

Table 2 describes the antenna positions for the four antenna array configurations 2) to 5). In configuration 1), the pairs of antennas 1–4, 2–3 and 5–6 are, respectively, L_x, L_y and L_z distant from each other, where $L_x = 0.76$ m, $L_y = 1.2$ m and $L_z = 0.3$ m and each pair is, respectively, aligned with the $\boldsymbol{x}$, $\boldsymbol{y}$, $\boldsymbol{z}$ from S_b.

As described in Section 6, we obtain the normalized phase shifts from chosen pairs of antennas. Table 3 shows the evaluated antenna pairs configurations, with cases a) and b) using a four antenna array and cases c) and d) using a six antenna array configuration.

Table 4 fully describes each antenna configuration, and name each configuration as it is referred in simulation results plots.

The base station transmits a narrowband signal with frequency $f = 30$ kHz. The antenna array receives this signal corrupted by a zero mean white Gaussian noise. The antenna array provides DOA estimates at 100 Hz calculated using ESPRIT according to Section 5. To calculate a DOA estimate, each antenna collects N_{samples} measurements at sample frequency of $f_s = 1/[f \cdot (N_{\mathrm{samples}} - 1)]$. $N_{\mathrm{samples}} = 64$ in all scenarios, except by the first one, which is $N_{\mathrm{samples}} = 1024$. For the sake of simplicity, the sampled signals are already in analytical (complex) form. The received data is simu-

Table 4

Full description of antenna array configurations.

Config.[a]	Name[b]	Description
1-c	6 ant. or 3	6-antenna, 3 measured phase shifts
1-d	6	6-antenna, 6 measured phase shifts
2-a	4 ant.	The simplest 4-antenna configuration
2-b	Phase	Same as 2-a, but unusual phase shift choice
3-b	Alternative	Alternative orthogonal antenna positioning
4-a	Rotated	Orthogonal positioning, rotated from S_b
5-a	$\beta = \ldots$	Non-orthogonal positioning

[a] See Tables 2 and 3 for configuration descriptions.
[b] Short name shown in plot legends.
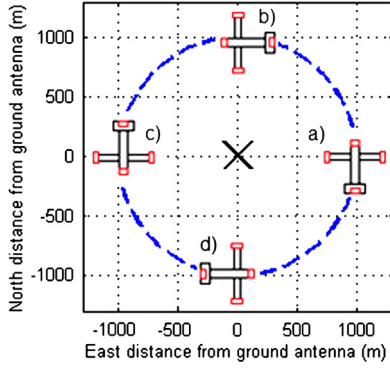
Fig. 14. Trajectory 1 viewed from above. The central cross is the base station position and the circle is the UAV trajectory. The UAV starts at position (1000,0), i.e., at a), and rotates counter-clockwise. At 12.5 s it is at b), at 25 s is at c), at 37.5 s is at d), and completes a full circle at 50 s.

lated for different signal-to-noise ratios (SNRs), which are defined as:

$$\text{SNR} = 10 \log_{10} \left(\frac{\sigma_s^2}{\sigma_n^2} \right), \tag{72}$$

where σ_s^2 and σ_n^2 are the signal and noise variances, respectively.

Two trajectories are simulated. In the first one, from [24], the UAV is flying around the base station in a circular path of radius 1000 m at constant speed starting at angle 0° as shown in Fig. 14. The speed is calculated to make the UAV complete the circle in 50 seconds. The UAV $\boldsymbol{x}_b$ axis and velocity vector are always tangent to the trajectory circle, i.e. the UAV flies without sideslip and the yaw is uniformly changing. The UAV flies with constant altitude (100 meters above the base station) with constant pitch of 0 rad. The roll angle is constant and equal to $-\pi/6$ rad.

Note that the trajectory assumed in [24] is very simplistic from the ESPRIT perspective, since the true phase shifts are constant all over the simulation and the distance between the UAV and the base station is constant.

Since this work improves the EKF from [24] to be tuned in real-time, the algorithms here are tested in a more complex scenario. In the new simulated trajectory, the phase shift between each pair of antennas and the distance between the UAV and the base station varies with time. The UAV starts at the same position: 100 m above from the ground and 1000 m west from the base station. The yaw, pitch and roll angles are described, respectively, as (angles in degrees):

$$\psi = -45°, \tag{73}$$

$$\theta = 360 \cdot \frac{t}{50} - 5 \cos(360/5 \cdot t), \tag{74}$$

$$\phi = 360 \cdot \frac{t}{5} - 2 \cos(360 \cdot t). \tag{75}$$

The speed of the UAV is constant and equal to 50 m/s. Like the first trajectory, the UAV $\boldsymbol{x}_b$ is aligned with the tangent of the trajec-

tory. The trajectory positions and attitude are depicted in Fig. 15. Note that, when $\theta = 90°$, which is the maximum allowed θ angle, the UAV is upside down, which instantly changes ψ to $-\psi$ and ϕ to $-\phi$. This type of discontinuity can occur when using Euler angles. The movement, however, is continuous.

The angular displacement I_k for each algorithm is calculated using

$$I_k = \left| \arccos \left(0.5 \, \text{trace} \left(D_b^{\text{NED}} \cdot \hat{D}_{\text{NED}}^b \right) \right) - 0.5 \right|, \tag{76}$$

where D_b^{NED} is the true DCM and $\hat{D}_{\text{NED}}^b$ is the transpose of the estimated one. If the estimate is perfect, I_k results in zero, and I_k is greater if the estimation is worse. The maximum value of I_k is 180°.

The TRIAD, QUEST and the EKF were tested in all antenna configurations, except in the first and in the lat one, where only the EKF performance is relevant. Results are shown by using $\bar{I}_k$, which is the mean of I_k from 500 Monte Carlo trials in each case.

Note that the EKF estimator is more sophisticated than QUEST, which is more sophisticated than TRIAD. While the EKF makes use of a system model, this is not the case of TRIAD or QUEST. Furthermore, the EKF and QUEST use information about the uncertainty of measurements, which is not the case of TRIAD. As expected, in all scenarios the EKF outperforms QUEST, which outperforms TRIAD. In the next plots, the TRIAD and QUEST plots are plotted side-by-side in the same scale, which allows an easy comparison between TRIAD and QUEST results. The EKF results are plotted with a different scale from TRIAD and QUEST, since the EKF performance is significantly better.

The results are presented in Subsections 7.1 to 7.6. In Subsection 7.1, the tuning method proposed in [24] is compared with our new proposed tuning method, using the 6-antenna array from Fig. 7, both presenting similar results. In Subsection 7.2, the performance of all orthogonal and S_b-aligned array configurations, Figs. 7, 9, and 10, and Fig. 9 with alternative choice of pairs of antennas are compared, presenting similar results. Subsection 7.3 uses the same scenario from Subsection 7.2, but with one antenna receiving a noisier signal. The array configurations in which antenna reuse is lower when choosing antenna pairs perform better. In Subsection 7.4, the 4-antenna orthogonal S_b-aligned configuration from Fig. 9 is compared with the orthogonal S_b-misaligned configuration from Fig. 11 and with non-orthogonal configurations based on Fig. 13. The orthogonal arrays perform similar, and the use of a non-orthogonal array implies in a performance cost. In Subsection 7.5, the use of six pairs of antennas instead of tree provides an increase of performance in the 6-antenna configuration from Fig. 7 in a low SNR scenario. Finally, Subsection 7.6 shows that the reduction of frequency in which the array provides LOS vector measurements to the EKF implies in a tolerable performance degradation.

7.1. Ad-hoc tuning versus real-time tuning

Fig. 16 shows the mean performance of two alternative tuning methods for the EKF-based algorithm over time, the *ad-hoc* method from our previous work [24], and by our new proposed method described in Subsection 5.2. The simulation parameters are described in the simulation scenario number 1 in Table 4, while the sensors are described in Table 1. TRIAD and QUEST results are not shown, since the main objective is to evaluate the EKF tuning methods.

Both EKF variants in Fig. 16 have a performance degradation around 12.5 and 37.5 seconds. As discussed in [24], this is related to an alignment between the north direction and LOS. In order to remove such performance degradation, a new measurement vector
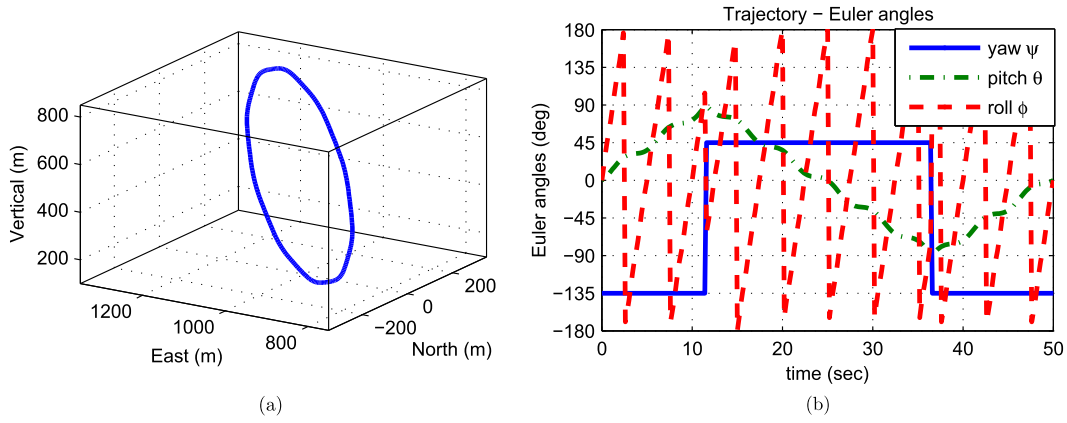
Fig. 15. Trajectory 2, where (a) and (b) are, respectively, the UAV position and attitude. The north, east and vertical labels indicate the distance from the UAV to the base station, in S_{NED}.
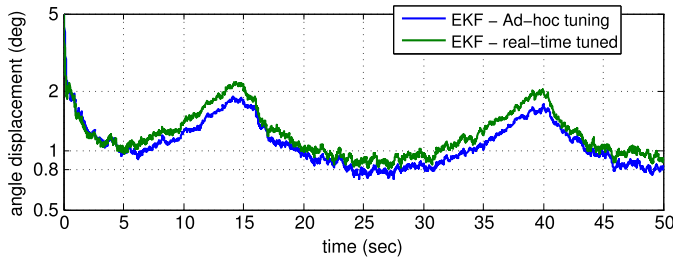

Fig. 16. Mean performance criterion I_k from scenario number 1 from Table 4.

Table 5
Simulation scenarios.

N.	Traj.	SNR (dB)	$N_{samples}$	Antenna configurations[a]	Extra description
1	1	0	1024	1-c	Two EKF tuning methods, *ad-hoc* and in real-time
2	2	20	64	1-c, 2-a, 3-b, 2-b	–
3	2	20	64	1-c, 2-a, 3-b, 2-b	Antenna 1 SNR is 10 dB lower
4	2	20	64	2-a, 4-a, 5-a	–
5	2	0	64	1-c, 1-d	–
6	2	20	64	2-a	Array LOS sample rate reduced to 1 Hz

[a] See Table 4.

not aligned with the LOS should be added. This should be obtained from another sensor, as accelerometer or camera.

Comparing the two EKF variants, note that both have similar performance with the *ad-hoc* approach performing slightly better. However, the *ad-hoc* approach consists in fine tuning the expected phase shift estimation error covariance to a very specific scenario by simulating this scenario hundreds of times and evaluating the ESPRIT performance. Such fine tuning approach is unrealistic, since the UAV must follow a pre-determined path to guarantee the performance of the estimator. Our new real-time tuning method from Subsection 5.2, however, does not have any previous knowledge about the scenario calculating on-the-fly the estimated phase shift error covariance and adapting according, if necessary. This new tuning method is used on the next simulated scenarios.

7.2. The 4-antennas orthogonal configurations

Here, all 4-antenna orthogonal configurations (simple, alternative and unusual phase shift) are simulated and compared with the 6-antenna configuration. The EKF is tuned in real-time (Section 5.2). The main objective is to evaluate if the reduced hardware cost of using less antennas implies in performance degradation in an usual scenario. The four evaluated configurations are described by scenario number 2 in Table 5.

The $N_{samples}$ was reduced from the first scenario, since the real-time tuning is computationally costly, and the cost increases significantly with the amount of samples. The SNR was slightly increased to compensate the reduction of samples. This change is made in all subsequent simulations. In a real scenario, the SNR is not adjustable, but the amount of samples is. The amount of samples can be increased to improve the results, if the UAV has a compatible computational power. An alternative approach is to calculate the tuning less often. For instance, one tuning can be performed after 10 phase shift estimations, and can be assumed that the scenario does not change so much between each tuning.

Fig. 17 shows the obtained results. Note that changing from 6 to 4 antennas does not significantly affect the attitude estimation performance in any of the estimators. The alternative and unusual phase shift configurations are proposed to minimize the degradation of performance when there is a faulty antenna. Since this is not the case in this scenario, the different configurations perform similarly.

7.3. The four-antenna orthogonal configurations with a single highly noisy antenna

As an evaluation of fault tolerance of a noisy antenna reception, the scenario number 3 from Table 5 reduces the SNR of the first antenna to 10 dB, which is 10 dB lower than the other antennas. The results are shown in Fig. 18.

The usual four antenna configuration relies heavily on the first antenna, since all of the three phase shifts are between the first antenna and another one. This results in a performance degradation of the estimation. The other four antenna configurations rely less on the first antenna, since each one uses the first antenna in only two of the three phase shifts measurements, whereas the 6 antenna configuration only uses the first antenna in one of three phase shifts estimations. The alternative phase shift configuration provides better noise tolerance in the EKF estimator, whereas the alternative configuration provides better noise tolerance in the TRIAD and QUEST estimators. The 6-antennas configuration attenuates the performance degradation caused by the faulty antenna in all estimators.
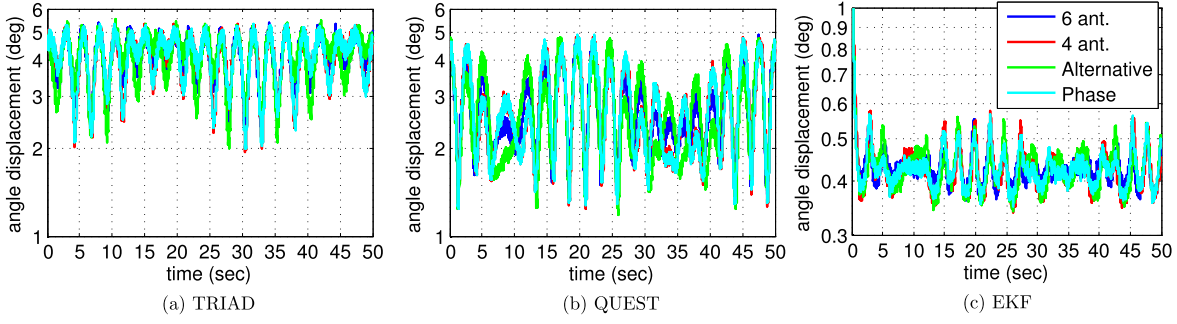
Fig. 17. Mean performance criterion I_k from scenario number 2 from Table 5. For each estimator, the results from all configurations are almost indistinguishable.
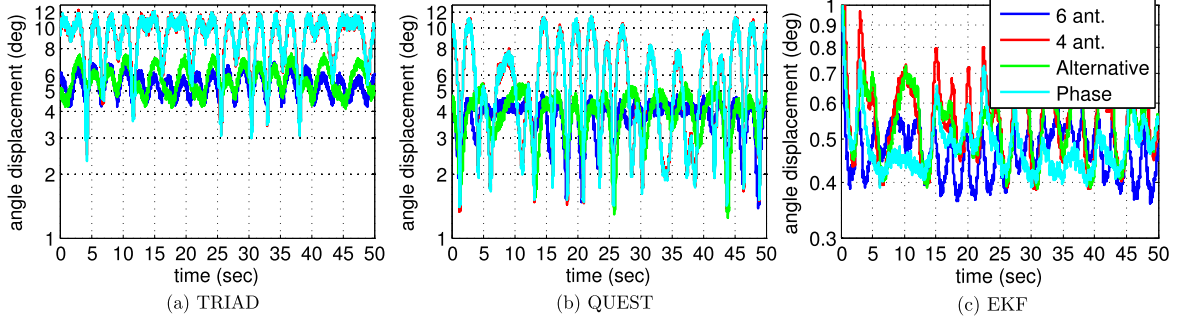

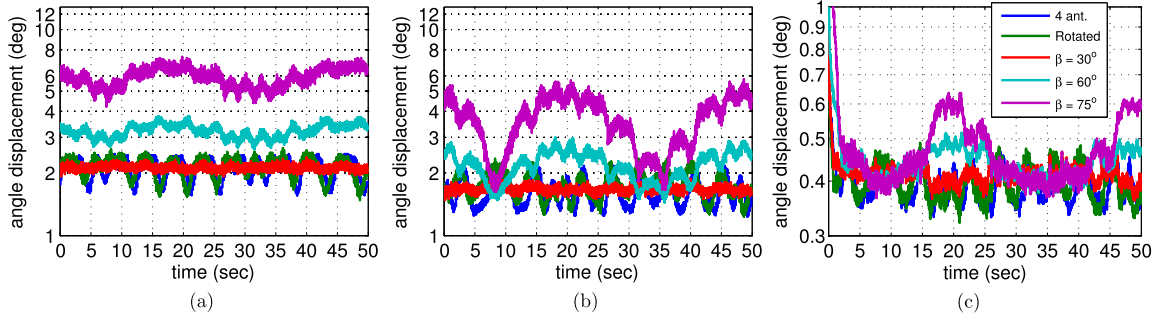**Fig. 18.** Mean performance criterion I_k from scenario number 3, where one antenna has noisier reception.

Fig. 19. Mean performance criterion I_k from scenario number 4.

7.4. Orthogonal versus non-orthogonal configurations

Here, the simple 4-antenna orthogonal configuration is compared to the rotated and non-orthogonal configurations, as described by scenario number 4 in Table 5. L_x, L_y and L_z are changed all to 1 m, in all configurations to simplify the analysis and β equals to 30°, 60°, and 75° in configuration 5-a. The main objectives are to show that the rotated variation does not imply in performance gain or loss, and to evaluate the performance degradation caused by non-orthogonality.

Fig. 19 shows the results from all estimator algorithms. The four antenna and rotated configurations perform very similarly, as expected. As the non-orthogonality increases, the performance becomes poorer. This shows that non-orthogonal antennas are possible, if a performance penalty is tolerable.

7.5. Using more than 3 phase shifts

Here, the configurations 1-c and 1-d from Table 4 are compared. The 1-c configuration uses 3 phase shifts, whereas 1-d uses 6 phase shifts, as described by scenario number 5 in Table 5. The SNR is changed to 0 dB, to amplify the difference between each configuration performance. The main objective is to verify if the use of extra phase shifts brings extra performance.

Figs. 20a and 20b show the results when using the TRIAD and QUEST estimators. In both cases, the 6 phase variant performs slightly better showing that the extra phase shifts bring new information to the estimator, even reusing antennas and creating extra vectors.

Fig. 20c shows the results when using the EKF estimator. In this case, the 6 phase variant works better only at the beginning and then performs slightly worse.

7.6. Use of lower LOS measurement sample rate

Up to this subsection, it is assumed that the antenna array is providing measurements at 100 Hz, which is the same sample rate as the magnetometer and gyro. However, the ESPRIT algorithm is way more complex than a simple capture of data from magnetometer or gyro. Here it is evaluated the effect of reducing the DOA estimate sample rate to 1 Hz, as a way to reduce the computational cost and, by extension, the energy cost. This is evaluated in scenario 6 from Table 5. The magnetometer and gyro measurement rate, and the EKF prediction and update steps, are maintained at 100 Hz. In EKF, at each 100 updates, 99 includes only the magnetometer one, and one includes both magnetometer and antenna array LOS estimate.
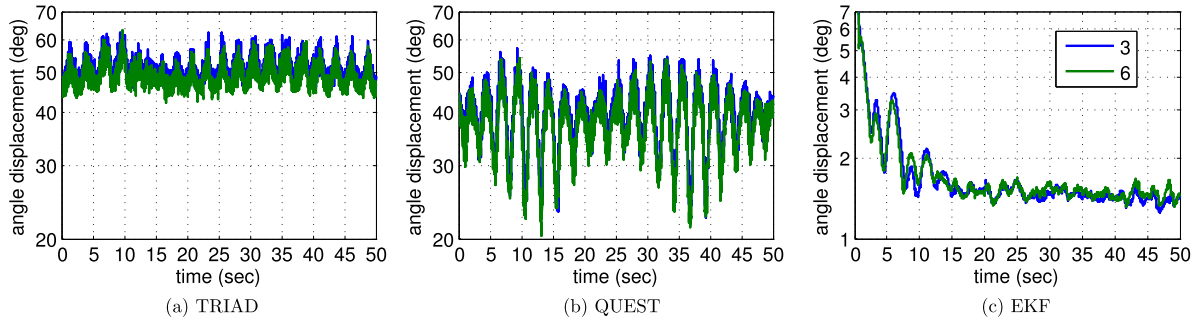
Fig. 20. Mean performance criterion I_k from scenario number 5, where the same configuration uses 3 or 6 phase shifts measurements.
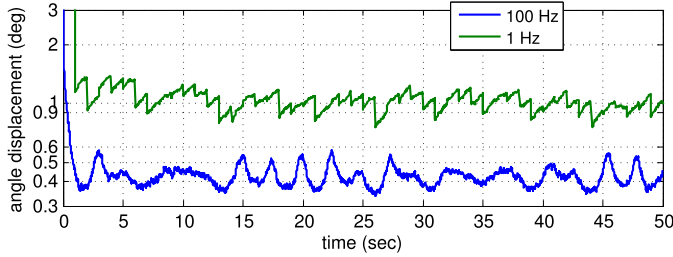

Fig. 21. Mean performance criterion I_k from scenario number 6, where a same antenna array configuration is evaluated at 1 Hz and 100 Hz. The lower sample time case provides, as expected, lower performance.

Fig. 21 shows the EKF results from the 100 Hz and 1 Hz sample rate. The 1 Hz version has a slight degradation as expected. In addition, a saw toot pattern is easily visible. Sensible increments in performance, i.e. sensible decrements at mean I_k, occurs at each second, when the antenna array LOS measurement is included in the update step of the EKF estimator. This result is expected, since the magnetometer alone does not provide full attitude information.

8. Conclusion

In this paper, an antenna array based attitude estimation framework is proposed. Phase shifts of a received signal between pairs of antennas are obtained via ESPRIT algorithm. Such estimates are represented as a LOS vector measurement, and incorporated into attitude estimation algorithms, such as TRIAD, QUEST or EKF. A real-time phase shift error covariance calculation algorithm is proposed. The framework is also expanded to arbitrary antenna array configurations.

The real-time noise covariance calculation algorithm allows similar performance to the previous *ad-hoc* approach in [24]. However, in contrast to the approach in [24], our new approach exploits the EKF in complex scenario characterized by variable parameters including the attitude, the relative distance between the UAV and the base station and/or the SNR without any type of configuration or parameter adjustment. Moreover, our approach facilitates the evaluation of several scenarios, since it does not require *ad-hoc* tuning the EKF for each scenario.

Several array configurations are analyzed and evaluated in simulations. The 4-antenna configuration performs similarly to the 6-antenna in [24], but using less antennas and resulting in lower cost. Other 4-antenna configurations, i.e., the rotated or the non-orthogonal, allow implementing the attitude estimator relaxing the restrictions on the antenna positions. Such procedure can be useful, for example, if the antennas are pre-installed, or if there is some limitation in the UAV structure, or if there is the need for dedicating energy to improve the communication. The unusual phase shift can help to find better estimation in specific scenarios, such as in scenarios with a faulty antenna. The use of extra phase shifts shows a slight improvement of the TRIAD and QUEST algorithms, but small performance degradation of the EKF. In other scenarios, the extra phase shifts cause degradation in both estimators. This shows that more research should be conducted for exploiting the cross correlation matrix of the extra phase shifts.

8.1. Improvements and future works

There are several interesting topics that can be pursued from this paper. The first one is the hardware implementation. Since the ESPRIT is based on the fast Fourier transform (FFT) to obtain the analytical signal, and EVD and singular value decomposition (SVD) calculation, a digital signal processor (DSP) is the most appropriate hardware to implement the ESPRIT algorithm. As an example, the *Overo WaterSTORM COM* computer-on-module [45] includes both an 1 GHz ARM Cortex-A8 processor and an 800 MHz DSP packed as a single chip *DaVinci DM3730*, and is compatible with the *Aerocore 2* micro-aerial-vehicle (MAV) control board [46]. This configuration allows the ESPRIT algorithm, the EKF, and the guidance and control algorithm of the UAV to execute, respectively, at the DSP, ARM, and MAV control board. As an example of the computational power of the proposed DSP, the 64-point FFT calculated in this paper to obtain the analytical signal can be calculated in 182 cycles [47], which results in around 23 μs when computing at 800 MHz.

Besides being a DSP capable of processing the ESPRIT algorithm, it is interesting to reduce the computational cost, since this allows the execution of other algorithms, and the reduction on energy consumption and reduction on hardware cost. The EVD cost of ESPRIT can be avoided by obtaining a signal subspace estimate by computationally efficient non-EVD methods. This can be made by recursive algorithms that can track the signal subspace, such as the projection approximation subspace tracking (PAST) algorithm [48] or by using a Kalman filter based subspace tracking approach [49], which also provides robustness when operating in impulsive noise environment. Such Kalman based approach returns a fast attitude estimation via TRIAD, which does not need the uncertainty estimation, and via QUEST, if the relative weight of sensors is tuned as off-line. The usage of cascade recursive filters provides sub-optimal or unstable results [50], therefore, the use of the PAST algorithm cascaded to the proposed EKF must be carefully evaluated.

The Kalman filter also needs the noise covariance estimate, which is calculated by using the SVD of a matrix. However, as verified during simulations in [24], this covariance is a function of the SNR and the true phase shift, which is related to the true attitude. By using this property, the usage of look-up table for several estimated phase shifts and SNR can avoid the real-time SVD calculation.

During hardware implementation, examples of sources of uncertainties are the positioning errors and the coupling of the antenna array elements. There are generalizations of the ESPRIT algorithm as well as interpolation schemes that can reduce these uncertainties as shown in [51–53].

Acknowledgments

Appendix A. Supplementary material

Supplementary material related to this article can be found online at http://dx.doi.org/10.1016/j.dsp.2016.07.006.

References

[1] M. Owen, R.W. Beard, T.W. McLain, Implementing Dubins airplane paths on fixed-wing UAVs, in: K.P. Valavanis, G.J. Vachtsevanos (Eds.), Handbook of Unmanned Aerial Vehicles, Springer, Netherlands, 2015, pp. 1677–1701.

[2] Y. Watanabe, Stochastically optimized monocular vision-based navigation and guidance, Ph.D. thesis, School of Aerospace Engineering, 2007.

[3] D.B. Wilson, A.H. Goktogan, S. Sukkarieh, A vision based relative navigation framework for formation flight, in: 2014 IEEE International Conference on Robotics and Automation, ICRA, IEEE, 2014, pp. 4988–4995.

[4] A. Fosbury, J. Crassidis, Relative navigation of air vehicles, J. Guid. Control Dyn. 31 (4) (2008) 824–834.

[5] D.B. Wilson, A.H. Göktogan, S. Sukkarieh, Guidance and navigation for UAV airborne docking, in: Proceedings of Robotics: Science and Systems, Rome, Italy, 2015, pp. 1–9.

[6] M.D. Shuster, S.D. Oh, Three-axis attitude determination from vector observations, J. Guid. Control Dyn. 4 (1) (1981) 70–77.

[7] E.J. Lefferts, F.L. Markley, M.D. Shuster, Kalman filtering for spacecraft attitude estimation, J. Guid. Control Dyn. 5 (5) (1982) 417–429.

[8] I.Y. Bar-Itzhack, Y. Oshman, Attitude determination from vector observations: quaternion estimation, IEEE Trans. Aerosp. Electron. Syst. AES-21 (1) (1985) 128–136, http://dx.doi.org/10.1109/TAES.1985.310546.

[9] T.F.K. Cordeiro, J. Waldmann, Covariance analysis of accelerometer-aided attitude estimation for maneuvering rigid bodies, in: VII Congresso Nacional de Engenharia Mecânica, ABCM, 2012, pp. 1–10.

[10] R.A.J. Chagas, J. Waldmann, Observability analysis for the INS error model with GPS/uncalibrated magnetometer aiding, in: D. Choukroun, Y. Oshman, J. Thienel, M. Idan (Eds.), Advances in Estimation, Navigation, and Spacecraft Control, Springer Verlag, 2015, pp. 235–257.

[11] M. Kok, J.D. Hol, T.B. Schon, F. Gustafsson, H. Luinge, Calibration of a magnetometer in combination with inertial sensors, in: 15th International Conference on Information Fusion, FUSION, 2012, pp. 787–793.

[12] E. Thébault, C.C. Finlay, C.D. Beggan, P. Alken, J. Aubert, O. Barrois, F. Bertrand, T. Bondar, A. Boness, L. Brocco, et al., International geomagnetic reference field: the 12th generation, Earth Planets Space 67 (1) (2015) 1–19.

[13] F. Lowes, The international geomagnetic reference field: a "health" warning, http://www.ngdc.noaa.gov/IAGA/vmod/igrfhw.html, 2010, accessed: 2016-05-10.

[14] H. Rehbinder, X. Hu, Drift-free attitude estimation for accelerated rigid bodies, Automatica 40 (4) (2004) 653–659.

[15] L.R. Lustosa, J. Waldmann, A novel imaging measurement model for vision and inertial navigation fusion with extended Kalman filtering, in: D. Choukroun, Y. Oshman, J. Thienel, M. Idan (Eds.), Advances in Estimation, Navigation and Spacecraft Control, Springer Verlag, 2015, pp. 275–289.

[16] H. Tong, S.A. Zekavat, A novel wireless local positioning system via a merger of DS-CDMA and beamforming: probability-of-detection performance analysis under array perturbations, IEEE Trans. Veh. Technol. 56 (3) (2007) 1307–1320.

[17] R. Zekavat, R.M. Buehrer, Handbook of Position Location: Theory, Practice and Advances, vol. 27, John Wiley & Sons, 2011.

[18] H. Liu, H. Darabi, P. Banerjee, J. Liu, Survey of wireless indoor positioning techniques and systems, IEEE Trans. Syst. Man Cybern., Part C, Appl. Rev. 37 (6) (2007) 1067–1080.

[19] S.T. Goh, O. Abdelkhalik, S.A.R. Zekavat, Differential geometric estimation for spacecraft formations orbits via a cooperative wireless positioning, in: 2010 IEEE Aerospace Conference, IEEE, 2010, pp. 1–11.

[20] S.T. Goh, O. Abdelkhalik, S.A.R. Zekavat, Spacecraft formation orbit estimation using wlps-based localization, Int. J. Navig. Obs. 2011 (2011).

[21] S.T. Goh, O. Abdelkhalik, S.A.R. Zekavat, A weighted measurement fusion Kalman filter implementation for UAV navigation, Aerosp. Sci. Technol. 28 (1) (2013) 315–323.

[22] J.P.C.L. da Costa, S. Schwarz, L.F.d.A. Gadêlha, H.C. de Moura, G.A. Borges, L.A.d.R. Pinheiro, Attitude determination for unmanned aerial vehicles via an antenna array, in: International ITG Workshop on Smart Antennas, WSA, 2012, pp. 264–268.

[23] K. Liu, J.P.C.L. da Costa, H.C. So, L.F.d.A. Gadêlha, G.A. Borges, Improved attitude determination for unmanned aerial vehicles with a cross-shaped antenna array, in: Proc. IASTED International Conference on Signal and Image Processing, SIP 2012, Honolulu, Hawaii, USA, 2012, pp. 60–67.

[24] T.F.K. Cordeiro, J.P.L.C. da Costa, K. Liu, G.A. Borges, Kalman-based attitude estimation for an UAV via an antenna array, in: 8th International Conference on Signal Processing and Communication Systems, ICSPCS, 2014, pp. 1–10.

[25] K. Liu, J.P.C.L. da Costa, H.C. So, F. Roemer, M. Haardt, L.F.d.A. Gadêlha, 3-D unitary ESPRIT: accurate attitude estimation for unmanned aerial vehicles with a hexagon-shaped ESPAR array, Digit. Signal Process. 23 (3) (2013) 701–711.

[26] F. Roemer, M. Haardt, G. Del Galdo, Analytical performance assessment of multi-dimensional matrix-and tensor-based ESPRIT-type algorithms, IEEE Trans. Signal Process. 62 (10) (2014) 2611–2625.

[27] C.D. Meyer, Matrix Analysis and Applied Linear Algebra, SIAM, 2000.

[28] B.L. Stevens, F.L. Lewis, Aircraft Control and Simulation, John Wiley & Sons, 2003.

[29] S. Maus, S. Macmillan, S. McLean, B. Hamilton, A. Thomson, M. Nair, C. Rollins, The US/UK world magnetic model for 2010–2015, Tech. rep., NOAA, 2010.

[30] R. Roy, T. Kailath, ESPRIT-estimation of signal parameters via rotational invariance techniques, IEEE Trans. Acoust. Speech Signal Process. 37 (7) (1989) 984–995, http://dx.doi.org/10.1109/29.32276.

[31] R.O. Schmidt, Multiple emitter location and signal parameter estimation, IEEE Trans. Antennas Propag. 34 (3) (1986) 276–280, http://dx.doi.org/10.1109/TAP.1986.1143830.

[32] C. Veness, Calculate distance, bearing and more between latitude/longitude points, http://www.movable-type.co.uk/scripts/latlong.html, 2015, accessed 04-May-2016.

[33] Mathworks, LLA to ECEF position, http://www.mathworks.com/help/aeroblks/llatoecefposition.html, 2014, accessed: 2014-06-22.

[34] O.S. Salychev, Applied Inertial Navigation: Problems and Solutions, BMSTU Press, Moscow, Russia, 2004.

[35] M.S. Andrle, J.L. Crassidis, R. Linares, Y. Cheng, B. Hyun, Deterministic relative attitude determination of three-vehicle formations, J. Guid. Control Dyn. 32 (4) (2009) 1077–1088.

[36] S.T. Goh, C.E. Passerello, O. Abdelkhalik, Spacecraft relative attitude determination, in: 2010 IEEE Aerospace Conference, 2010, pp. 1–6.

[37] M.D. Shuster, Constraint in attitude estimation part I: constrained estimation, J. Astronaut. Sci. 51 (1) (2003) 51–74.

[38] F.L. Markley, Attitude determination using two vector measurements, Tech. rep., NASA, 1998.

[39] S. Tanygin, M.D. Shuster, The many triad algorithms, in: AAS/AIAA 17th Space Flight Mechanics Meeting, Sedona, Arizona, 2007, pp. 81–99.

[40] A. Carmi, Y. Oshman, Asymptotic behavior of the estimation error covariance of quaternion estimators, J. Guid. Control Dyn. 31 (6) (2008) 1665–1676.

[41] J.P.C.L. da Costa, F. Roemer, M. Haardt, R.T. de Sousa Jr., Multi-dimensional model order selection, EURASIP J. Adv. Signal Process. 26 (2011) 1–13.

[42] J.P.C.L. da Costa, A. Thakre, F. Roemer, M. Haardt, Comparison of model order selection techniques for high-resolution parameter estimation algorithms, in: 54th International Scientific Colloquium, IWK, Ilmenau, Germany, 2009, pp. 1–6.

[43] K. Liu, J.P.C.L. da Costa, H.C. So, L. Huang, Subspace techniques for multidimensional model order selection in colored noise, Signal Process. 93 (2013) 1976–1987.

[44] S.J. Julier, J.K. Uhlmann, A non-divergent estimation algorithm in the presence of unknown correlations, in: Proceedings of the American Control Conference, 1997, pp. 2369–2373.

[45] Gumstix, Overo waterstorm com, https://store.gumstix.com/coms/overo-coms/overo-waterstorm-com.html, 2016, accessed: 2016-02-24.

[46] Gumstix, Aerocore 2 for overo, https://store.gumstix.com/aerocore-2-for-overo.html, 2016, accessed: 2016-02-24.

[47] Texas Instruments, DaVinci benchmarks product bulletin (rev. a), http://www.ti.com.cn/cn/lit/ml/sprt379a/sprt379a.pdf, 2006, accessed: 2016-02-24.

[48] B. Yang, Projection approximation subspace tracking, IEEE Trans. Signal Process. 43 (1) (1995) 95–107, http://dx.doi.org/10.1109/78.365290.

[49] B. Liao, Z.G. Zhang, S.C. Chan, A new robust Kalman filter-based subspace tracking algorithm in an impulsive noise environment, IEEE Trans. Circuits Syst. II, Express Briefs 57 (9) (2010) 740–744, http://dx.doi.org/10.1109/TCSII.2010.2056414.

[50] N. Carlson, Federated filter for fault-tolerant integrated navigation systems, in: Position Location and Navigation Symposium, 1988. Record. Navigation into the 21st Century, IEEE PLANS '88, IEEE, 1988, pp. 110–119.

[51] M.A.M. Marinho, J.P.C.L. da Costa, F. Antreich, L.R.A.X. de Menezes, Unscented transformation based array interpolation, in: IEEE International Conference on Acoustics, Speech and Signal Processing, ICASSP, 2015, 2015, pp. 2819–2823.

[52] M.A.M. Marinho, J.P.C.L.d. da Costa, F. Antreich, A.L.F. de Almeida, Multidimensional array interpolation applied to direction of arrival estimation, in: Proceedings of 19th International ITG Workshop on Smart Antennas, WSA 2015, 2015, pp. 1–6.

[53] B. Liao, S. Chan, Direction finding in partly calibrated uniform linear arrays with unknown gains and phases, IEEE Trans. Aerosp. Electron. Syst. 51 (1) (2015) 217–227, http://dx.doi.org/10.1109/TAES.2014.130460.

Thiago Felippe K. Cordeiro received the Diploma degree in automation and control engineering in 2009 from the University of Brasília (UnB), Brazil and the M.Sc. degree in electronic engineering and computer science in 2012 from the Aeronautics Institute of Technology (ITA), Brazil. Currently, he pursues a Ph.D. degree at the UnB with interests on navigation, guidance and control of unmanned aerial vehicles. Also, since 2013, he is a Aerospace Engineering Professor in the Faculdade do Gama Campus, at the University of Brasília, Brazil.

João Paulo Carvalho Lustosa da Costa received the Diploma degree in electronic engineering in 2003 from the Military Institute of Engineering (IME) in Rio de Janeiro, Brazil, his M.Sc. degree in telecommunications in 2006 from University of Brasília (UnB) in Brazil, and his Doktor-Ingenieur (Ph.D.) degree with Magna cum Laude in electrical and information engineering in 2010 at Ilmenau University of Technology (TU Ilmenau) in Germany. Since 2010, he coordinates the Laboratory of Array Signal Processing (LASP) and since 2014, he works as a senior researcher at the Ministry of Planning in projects related to Business Intelligence. He was a visiting scholar at University Erlangen-Nuremberg, at Munich Technical University, at Seville University, at Harvard University, at Ilmenau University of Technology and at Fraunhofer Institute for Integrated Circuits IIS. Currently he coordinates a project related to distance learning courses at the National School of Public Administration and a special visiting researcher (PVE) project related to satellite communication and navigation together with the German Aerospace Center (DLR) supported by the Brazilian government.

He is a Guest Editor for Hindawi International Journal of Antennas and Propagation, special issue on "MIMO Antennas in Radar Applications 2016" and he served as the general-chair of the International Conference on Cyber Crime Investigation (ICCyber), International Conference on Multimedia Forensics, Surveillance and Security (ICMEDIA) and International Conference on Forensic Computer Science (ICoFCS) in 2015. He has been named an IEEE Senior Member in Signal Processing in 2015. He obtained four best paper awards on the following conferences: IV IEEE International Conference on Ultra Modern Telecommunications and Control Systems (ICUMT'12), ICoFCS'12, ICoFCS'13 and ICoFCS'15.

Rafael Timóteo de Sousa Júnior was born in Campina Grande – PB, Brazil, on June 24, 1961. He graduated in Electrical Engineering from the Federal University of Paraíba – UFPB, Campina Grande – PB, Brazil, 1984, and got his Doctorate Degree in Telecommunications from the University of Rennes 1, Rennes, France, 1988. He worked as a software and network engineer in the private sector from 1989 to 1996. Since 1996, he is a Network Engineering Professor in the Electrical Engineering Department, at the University of Brasília, Brazil. From 2006 to 2007, supported by the Brazilian R&D Agency CNPq, He took a sabbatical year in the Group for the Security of Information Systems and Networks, at Ecole Superiéure d'Electricité, Rennes, France. He is a member of the Post-Graduate Program on Electrical Engineering (PPGEE) and supervises the Decision Technologies Laboratory (LATITUDE) of the University of Brasília. His field of study is distributed systems and network management and security.

Hing Cheung So was born in Hong Kong. He received the B.Eng. degree from City University of Hong Kong (CityU) and the Ph.D. degree from The Chinese University of Hong Kong (CUHK), both in electronic engineering, in 1990 and 1995, respectively. From 1990 to 1991, he was an Electronic Engineer at the Research and Development Division, Everex Systems Engineering Ltd., Hong Kong. During 1995–1996, he worked as a Postdoctoral Fellow at CUHK. From 1996 to 1999, he was a Research Assistant Professor at Department of Electronic Engineering, CityU, where he is currently a Professor. His research interests include detection and estimation, fast and adaptive algorithms, multidimensional harmonic retrieval, robust signal processing, source localization, and sparse approximation. He has been on the editorial boards of IEEE Signal Processing Magazine (2014–), IEEE Transactions on Signal Processing (2010–2014), Signal Processing (2010–), and Digital Signal Processing (2011–). In addition, he is an elected member in Signal Processing Theory and Methods Technical Committee (2011–) of the IEEE Signal Processing Society where he is chair in the awards subcommittee (2015–). He has been elected Fellow of IEEE in recognition of his contributions to spectral analysis and source localization in 2015.

Geovany A. Borges received both B.Sc. and M.Sc. degrees in electrical engineering from the Federal University of Paraíba – UFPB, Campina Grande – PB, Brazil, in 1996 and 1998, respectively. In 2002, he concluded his doctoral studies with the Robotics Department of the Laboratoire d'Informatique, de Robotique et de Microélectronique de Montpellier, France. In 2003, he received the 2001–2002 Club EEA prize for the best French thesis in automatic control. He is a Professor at the Electrical Engineering Department, Universidade de Brasília, in Brasília, Brazil, and the head of Automation and Robotics Laboratory (LARA). His current research are in the fields of terrestrial and aerial mobile robotics, medical robotics, computer vision, stochastic signal processing, and control systems.